AGU ADVANCING EARTH AND SPACE SCIENCES

JGR Space Physics

RESEARCH ARTICLE
10.1029/2024JA033429

Key Points:

- Epicenters of concentric traveling ionospheric disturbances (TIDs) and gravity waves (GWs) correspond to areas with high convective available potential energy in summer
- The epicenters of concentric TIDs and GWs in winter correspond to regions south of extratropical cyclones' centers
- Sixty six percent of the stratospheric concentric GW events occurred simultaneously with concentric TIDs

Supporting Information:

Supporting Information may be found in the online version of this article.

Correspondence to:

M. Kogure,
kogure.masaru.055@m.kyushu-u.ac.jp

Citation:

Kogure, M., Yue, J., Chou, M.-Y., Liu, H., Otsuka, Y., Randall, C. E., et al. (2025). Coincident/simultaneous observations of stratospheric concentric gravity waves and concentric traveling ionospheric disturbances over the continental U.S. in 2022. *Journal of Geophysical Research: Space Physics*, *130*, e2024JA033429. https://doi.org/10.1029/2024JA033429

Received 15 OCT 2024
Accepted 10 FEB 2025

Coincident/Simultaneous Observations of Stratospheric Concentric Gravity Waves and Concentric Traveling Ionospheric Disturbances Over the Continental U.S. in 2022

Masaru Kogure[1,2,3,4], Jia Yue[3,4], Min-Yang Chou[3,4], Huixin Liu[2], Yuichi Otsuka[5], Cora E. Randall[6], Lars Hoffmann[7], and Yuta Hozumi[3,4]

[1]Department of Atmospheric Sciences, Yonsei University, Seoul, South Korea, [2]Department of Earth and Planetary Science, Kyushu University, Fukuoka, Japan, [3]NASA GSFC, Greenbelt, MD, USA, [4]Catholic University of America, Washington, DC, USA, [5]Institute for Space-Earth Environmental Research, Nagoya University, Nagoya, Japan, [6]Laboratory for Atmospheric and Space Physics, University of Colorado Boulder, Boulder, CO, USA, [7]Jülich Supercomputing Centre, Forschungszentrum Jülich, Jülich, Germany

Abstract This study examines the seasonal distributions of simultaneous stratospheric concentric gravity waves (GWs) observed by the Atmospheric Infrared Sounders and concentric traveling ionospheric disturbances (TIDs) detected by the ground-based Global Navigation Satellite System Total Electron Content observations over the U.S. in 2022, to illustrate the mesoscale vertical coupling between the lower atmosphere and the ionosphere. We compared epicenters of GWs and TIDs in the stratosphere and ionosphere with tropospheric weather conditions and background winds in the thermosphere. Epicenters of concentric TIDs associated with stratospheric concentric GWs correspond to areas with high convective available potential energy over the central to eastern U.S. (∼60–110°W) in summer and over the southern U.S. (south of ∼40°N) in spring and fall. Conversely, in fall to spring, epicenters over the northern U.S. (north of ∼40°N) appeared south of regions with high extratropical cyclone activity. These findings suggest that convection was a primary source of concentric GWs driving TIDs over the continental U.S. during all four seasons, although the specific weather phenomena associated with the convection varied by season. Convection over the central to eastern U.S. in summer and the southern U.S. in spring could be linked to thunderstorms. In contrast, convection over the northern U.S. from fall through spring was likely linked to extratropical cyclones. We also found that concentric TIDs were linked to 66% of the stratospheric concentric GW events (195 events in total), underscoring the significant role of convection as a source of TIDs in the lower atmosphere and its contribution to the vertical coupling.

1. Introduction

Traveling ionospheric disturbances (TIDs) are plasma density fluctuations in the ionosphere (Hines, 1964; Hunsucker, 1982; Hocke & Schlegel, 1996; Y. Otsuka, 2021). There are two types of TIDs defined by their generation mechanisms. One type is caused by gravity waves (GWs), which are a neutral atmosphere wave generally generated in the lower atmosphere and propagate into the upper atmosphere, transporting their momentum and energy (Hines, 1960). When GWs reach the thermosphere, they induce neutral-ion collision in the ionosphere, driving TIDs (Hines, 1960; Kotake et al., 2007; Nicolls et al., 2014; Oliver et al., 1997; Tsugawa et al., 2004; Vadas & Liu, 2009). GW-type TIDs can propagate omnidirectionally during both daytime and nighttime, although they prefer to propagate opposite to the background wind direction (Cowling et al., 1971; Crowley et al., 1987; Crowley & Rodrigues, 2012). The other mechanism involves perturbations of polarization electric fields induced by Perkins instability (Kelley & Miller, 1997; Miller et al., 1997; Otsuka et al., 2007; Perkins, 1973; Saito et al., 1998; Shiokawa et al., 2003). Perkins instability-type TIDs propagate only westward, with plane wavefronts, and equatorward along geomagnetic field lines during nighttime in both hemispheres and primarily occur during solstices and solar minimum conditions. These differences enable us to distinguish between GW-type and Perkins instability-type TIDs.

Several studies have shown that potential sources of GWs driving TIDs include earthquakes, volcanic eruptions, tropical cyclones, tsunamis, thunderstorms, jets/fronts, and secondary/tertiary GW generation in the middle atmosphere (Azeem et al., 2017; Chou et al., 2016; Heale, Bossert, & Vadas, 2022; Heale, Inchin, & Snively, 2022; Hung & Kuo, 1978; Kogure et al., 2024; Liu et al., 2011; Miyoshi et al., 2018; Nishioka et al., 2013; Takahashi et al., 2022; Taylor & Hapgood, 1988; Vadas & Azeem, 2021; Vadas & Crowley, 2010; Vadas & Liu, 2009, 2013; Vadas et al., 2023; Wright et al., 2022; Yang et al., 2022). Other potential sources of GWs driving TIDs include heating related to auroral processes during geomagnetic storms in the thermosphere (Chimonas & Hines, 1969; Ding et al., 2007; Hocke & Schlegel, 1996) and impacts of rocket launches (Afraimovich et al., 2002; Arendt, 1971; Bowling et al., 2013; Calais & Minster, 1996; Chou et al., 2018; Ding et al., 2014; Kakinami et al., 2013; Li et al., 1994; Lin, Chen, et al., 2017; Lin et al., 2014; Noble, 1990). GWs generated by joule heating and auroral particle precipitation tend to induce LSTIDs (large-scale TIDs) propagating equatorward from auroral zones in both hemispheres (Richmond, 1978).

Convection (e.g., related to tropical cyclones and thunderstorms) is one of the primary sources of GWs. There are three GW generation mechanisms within convection: pure thermal forcing, a mechanical oscillator effect, and an obstacle effect (Fritts & Alexander, 2003). The obstacle effect generates GWs propagating opposite to the background wind relative to the convective obstacle (Clark et al., 1986; Pfister & Russell, 1993; Pfister et al., 1993). On the other hand, thermal forcing and the mechanical oscillator effect generate concentric GWs because of the localized point source (Piani et al., 2000). GWs/TIDs from convective sources through the thermal forcing and mechanical oscillator effect mechanisms show concentric wave patterns, allowing us to distinguish them from waves from other sources (spontaneous adjustments and flow over mountains). In addition, the geographic location of the generation of concentric GWs can be relatively easily detected because their epicenters correspond to the generation points. It should be noted that an apparent epicenter would deviate a few hundreds of kilometers from its generation point if the background wind is strong (Kogure et al., 2020; Vadas et al., 2009). Concentric GWs propagate into the thermosphere, with anisotropies occurring due to background wind filtering effects, and then generate partially concentric TIDs in the ionosphere (Kim et al., 2009; Vadas, 2013; Vadas & Fritts, 2004). Concentric GWs are also generated by the secondary wave generation mechanism, that is, local body force, which is one of the important GW sources in the thermosphere (Vadas, 2013; Vadas & Liu, 2009).

Previous papers have shown that high convective activities can simultaneously generate concentric GWs in the stratosphere and concentric TIDs (Azeem et al., 2017; Chou et al., 2016; Srinivasu & Dashora, 2024). These coincidences allow for the identification of potential GW and TID sources as the same convection cell in the troposphere. However, no studies have shown the geographical distribution and seasonal variations of these simultaneous events nor the correlation between the events and meteorological conditions. Due to the lack of such studies, it is not well known what meteorological characteristics/parameters are strongly connected to the occurrence of concentric TIDs driven by GWs propagating directly from the troposphere. TIDs affect the precise processing of Global Navigation Satellite Systems (GNSS) (Hernández-Pajares et al., 2006, 2007) and high-frequency communication systems (Bristow et al., 1994; Frissell et al., 2014; Samson et al., 1989). Thus, understanding the generation mechanism of TIDs is critically important for maintaining wireless communication technologies.

This paper investigates the statistical distributions of simultaneous concentric GWs' and TIDs' epicenters over the continental U.S. during the four seasons of 2022 (a solar medium year: F10.7 = 100–150 sfu). Section 2 introduces the observation techniques: two satellites (Atmospheric Infrared Sounders (AIRS) and Aeronomy of Ice in the Mesosphere (AIM)) observing stratospheric GWs and Global Navigation Satellite System Total Electron Content (GNSS-TEC) observing TIDs. The continental U.S. has extensive TEC coverage with more than 6,000 GNSS receivers, which is advantageous for capturing concentric TID structures in GNSS-TEC data. Section 3 describes an analysis used to classify concentric GW and concentric TID events. Section 4 shows the distribution and local time variation of epicenters of stratospheric concentric GWs and concentric TIDs. Section 5 presents the weather conditions over the continental U.S. in 2022, discussing the potential sources of concentric TIDs associated with stratospheric GWs. Section 6 compares the distribution and local time variation of background winds to those of the epicenters. Section 7 concludes this paper.

2. Observations of Concentric GWs and Concentric TIDs

2.1. Concept of Atmospheric Vertical Coupling and Corresponding Observations

Figure 1 shows a schematic of mesoscale wave vertical coupling between the lower atmosphere and ionosphere and the corresponding observations presented in this paper. Convection generates concentric GWs in the troposphere that propagate into the stratosphere, where anisotropies of GWs occur due to the strong stratospheric jet. These stratospheric GWs are captured by both AIRS and Cloud Imaging and Particle Size Instrument (CIPS).

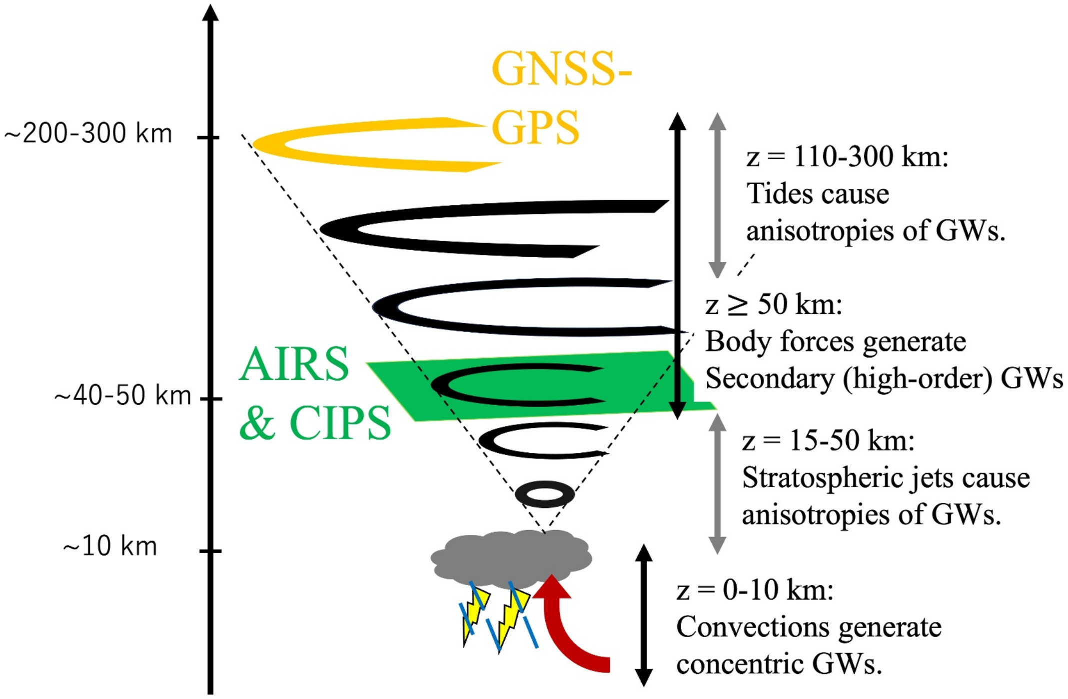

Figure 1. A schematic of mesoscale atmospheric wave vertical coupling and its observation.

When the upward propagating GWs reach the thermosphere/ionosphere, their frequencies are Doppler shifted due to tidal winds and mean winds. GWs decrease in their frequencies and vertical wavelengths when their propagation direction of GWs aligns with the background wind (tidal wind + mean wind), leading to wave breaking and anisotropies in GWs. The GWs that survive from the stratosphere to the thermosphere/ionosphere can drive partial concentric TIDs captured by the ground-based GNSS-TEC observations. In another vertical path, convectively-generated concentric GWs break due to strong wind, which generates concentric secondary GWs. These secondary and higher-order GWs also reach the thermosphere/ionosphere, generating concentric TIDs (Azeem & Barlage, 2018; Vadas & Azeem, 2021; Vadas & Crowley, 2010).

2.2. Atmospheric Infrared Sounder (AIRS) and Cloud Imaging and Particle Size Instrument (CIPS)

AIRS is an instrument aboard the NASA Aqua satellite launched on 4 May 2002 (Aumann & Pagano, 2003; Chahine et al., 2006). Aqua has a sun-synchronous orbit at an altitude of ~705 km, orbiting the Earth every 98.8 min and crossing the equator going north at ~1:35 p.m. LT and going south at ~1:35 a.m. LT. AIRS measures infrared radiance spectra in three spectral bands between 3.74 and 15.4 μm. AIRS uses cross-track scanning, with each scan consisting of 90 footprints over 1,780 km of ground distance and an along-track distance of 18 km. The footprint size ranges from 14 × 14 km^2 at the nadir to 21 × 42 km^2 at the edges of the scan. We analyzed dedicated AIRS 15μm brightness temperature data sets provided by the Jülich Supercomputing Center, Germany (Hoffman, 2021. https://datapub.fz-juelich.de/slcs/airs/gravity_waves/), to investigate concentric GWs over the continental U.S. in the stratosphere. The method to derive GW perturbations is as follows. First, the brightness temperatures observed in two AIRS channels were averaged using kernel functions peaking topmost at 40–45 km of altitude and full widths at half maximum of ~15 km to reduce measurement noise. Second, the background temperatures, calculated by a fourth-order polynomial fit, were subtracted for each across-track scan. The remaining brightness perturbations provide a measure of GWs with vertical wavelengths longer than ~15 km and horizontal wavelengths between ~50 and 500 km. The AIRS observations and retrieval of GWs are described in more detail by Hoffmann et al. (2013, 2014, 2017).

We also analyzed Rayleigh scattering albedo anomaly (RAA) from CIPS on the NASA Aeronomy of Ice in the Mesosphere (AIM) satellite (McClintock et al., 2009; Rusch et al., 2017). CIPS is one of three instruments on the NASA AIM satellite, which was launched in 2007 into a near-polar, sun-synchronous orbit at an altitude of

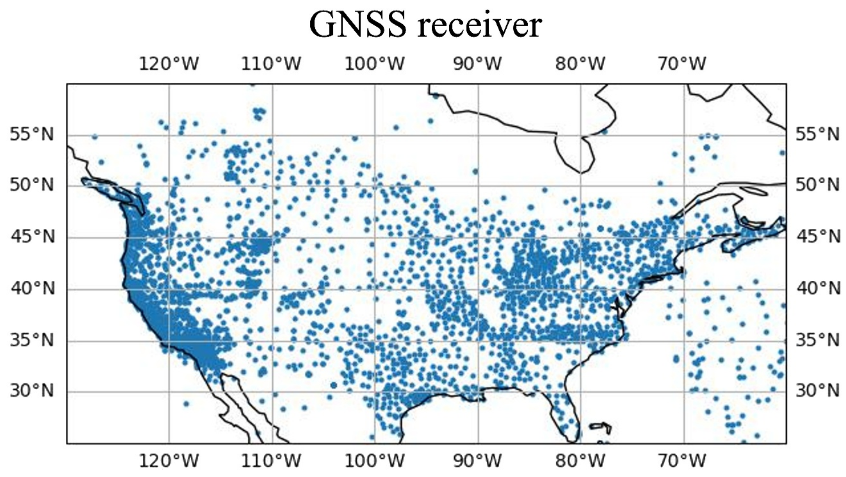

Figure 2. Map of Global Navigation Satellite Systems receivers on 1 January 2022.

~600 km (McClintock et al., 2009; Russell III et al., 2009). CIPS is a four-camera, nadir-viewing panoramic imager that measures 265-nm radiation scattered by the neutral atmosphere as well as by polar mesospheric clouds (PMCs) with 7.5 × 7.5 km^2 horizontal resolution, which is a few times higher than that of AIRS. Since the GNSS-TEC coverage area in this study is from ~25° to 50°N, PMC scattering can be neglected. The source function of the 265-nm radiation observed by CIPS peaks at an altitude of 50–55 km (Bailey et al., 2009), ~10 km higher than the most sensitive altitude of AIRS (40–45 km). We used the CIPS Rayleigh Albedo Anomaly data product provided by the University of Colorado Laboratory for Atmospheric and Space Physics (https://lasp.colorado.edu/aim/download). The background Rayleigh albedo, which is the albedo that would be observed in the absence of small-scale atmospheric perturbations such as GWs, is calculated using a numerical generalization of the "C-σ" model described in Carstens et al. (2013). The RAA, which at the scales of interest here is interpreted as being due to GWs, is then calculated by subtracting the background albedo from the observed Rayleigh albedo (Randall et al., 2017). The methodology and retrieval of the RAA are described in Carstens et al. (2013) and Randall et al. (2017).

CIPS captures GWs with horizontal wavelengths ranging from ~15 to 600 km and vertical wavelengths longer than ~15 km, similar to AIRS. However, CIPS has a cross-track coverage of ground distance (~1,000 km) that is half of that of AIRS, sometimes preventing us from detecting concentric GWs and determining their epicenters. Also, CIPS can observe GWs once-a-day (sunlit only). The observable local time is generally at ~12 LT in 2022, although the local time has changed over the course of the mission. Because of its narrow coverage and its low sampling frequency, the number of concentric GW events in CIPS is generally 2–5 times lower than in AIRS. Regardless of its narrow coverage, Xu et al. (2024) reported that temporal and geographical variations of GWs in CIPS are consistent with those in AIRS. Although this paper does not discuss the results of CIPS, they are shown in Figures S3–S5 in Supporting Information S1. In general, they are similar to the distributions of concentric GWs observed by AIRS, which strengthens the robustness of our results.

2.3. Global Navigation Satellite System Total Electron Content (GNSS-TEC)

The GNSS-TEC data are obtained from many ground-based GNSS receivers worldwide, and this study used data from the continental U.S (Figure 2). The continental U.S. has dense coverage with more than 6,000 receivers covering ~60–130°W, ~25–60°N. In particular, the dense GNSS-TEC data are available in the areas of 70–130°W, 30–50°N. We applied an elevation mask of 15°, smoothed TEC data from each receiver over 15 min, and subtracted the smoothed TECs from the unsmoothed TECs. Because the 15-min running window has a full width at half maximum of ~25 min, the detrended TEC data retain Fourier components with periods shorter than ~25 min, excluding LSTIDs induced by auroral joule heat. Then, all the detrended TEC data were binned into 0.25° × 0.25 ° × 30-s grid boxes to construct the GNSS-TEC maps. The remaining detrended TEC signals are defined as TIDs, whose spectral ranges are ground-based periods of 1–25 min and horizontal wavelengths more than the Nyquist number (0.5°, i.e., ~60 km). We estimate the minimum observable TID vertical wavelength to be of the order of ~100 km because GNSS receivers can only observe vertically integrated total electron content (up to several thousands of km). Considering the limitation of the period-band and horizontal resolution, the minimum ground-based phase speed is ~40 ms^{-1} (=0.5°/~25 min). Given the wide coverage and high temporal and spatial resolution provided by these data, this type of statistical study can only be carried out over the continental U.S. so far.

3. Analysis

We classified concentric GW and concentric TID events during 2022 into three categories: (a) concentric TIDs in GNSS-TEC associated with concentric GWs captured by AIRS (AIM) simultaneously, (b) concentric GWs only observed in AIRS (AIM), and (c) concentric TIDs only observed in GNSS-TEC. The concentric GWs, concentric TIDs, and their apparent epicenters were estimated through visual inspection. Estimated locations of epicenters typically vary by less than 1–2° among investigators. There are several techniques (beam-forming, raytracing, and circle method) that are commonly used by seismologists to locate the epicenters of earthquakes and can also be applied to identify the epicenters of TIDs (Liu et al., 2011). However, these methods require assumptions about generation altitude, non-background wind conditions, and constant group velocity, which sometimes lead to errors. This study analyzed 84 days in spring, 92 days in summer, 91 days in fall, and 87 days in winter in daytime (354 days in total). For nighttime, the numbers of days analyzed are the same as nighttime, except in spring (85 days); that is, the total number is 355 days. The simultaneous case, category (a), is defined as GNSS-TEC capturing concentric TIDs within ±3-hr of the time when AIRS (CIPS) captured concentric GWs, with the horizontal distance less than ~5° between both apparent epicenters. Due to vertical propagation lags and different observable GW spectra, AIRS (CIPS) and GNSS-TEC might not capture the exact same wave packet, but both wave sources are most likely the same (Yue et al., 2013, 2014).

Figure 3 shows examples of the three categories. The top panels (a, b) show a simultaneous event in AIRS and GNSS-TEC, the middle panels (c, d) show a concentric GW-only event in AIRS, and the bottom panels (e, f) show a concentric TID-only event in GNSS-TEC. Partial concentric GWs and TIDs are clearly visible within the black rectangle in Figures 3a and 3b, with epicenters for the GWs and TIDs located at ~87°W, ~37°N, and ~87°W, ~35°N, respectively. On the other hand, partial concentric GWs with an epicenter at ~102°W, ~47°N were present over the central U.S. in Figure 3c, while there were no TIDs similar to those GWs, although some TIDs propagated northward from the south in Figure 3d. In contrast, concentric TIDs in Figure 3f were visible over the West Coast, with their epicenter at ~113°W, ~28°N, but there were no GWs in Figure 3e. As a result, the evidence of vertical coupling for the TID-only event is not established. This paper focuses primarily on simultaneous GW and TID events (category 1) and GW-only events (category 2), as AIRS may have missed capturing some GWs due to its sparse sampling and limited observable GW spectra, which introduces significant ambiguity in identifying their potential sources. Examples of the three categories for CIPS are shown in Figure S1 in Supporting Information S1.

Although we can distinguish concentric TIDs from other TIDs, large-amplitude TIDs may obscure concentric TIDs. In particular, TIDs driven by Joule heating tend to have large amplitude during high-active geomagnetic storms. Geomagnetic high-activity events (with a 3-hourly Kp index of 4–7) are included when we can identify the epicenters of concentric TIDs superimposed with TIDs driven by Joule heating. However, large-amplitude TIDs driven by Joule heating may obscure concentric TIDs, potentially affecting the observed seasonal variation. To assess the frequency of TIDs driven by Joule heating each season, we analyze occurrence rates of a Kp index higher than 4. The occurrence rates were 9% in winter, 6% in spring, 8% in summer, and 9% in fall. Since the variation in each season is quite small, the obscuration effect does not impact the discussion in Chapters 5 and 6.

It should be noted that concentric TIDs caused by rocket launches on the West and East coasts were excluded. The locations include Cape Canaveral Space Force Station (80°W, 28°N), John F. Kennedy Space Center (80°W, 28°N), Vandenberg Space Force Base (121°W, 35°N), Mid-Atlantic Regional Spaceport (75°W, 38°N), Wallops Flight Facility (75°W, 38°N), White Sands Missile Range (106°W, 32°N), White Sands Missile Range (106°W, 32°N), Corn Ranch (105°W, 31°N), Spaceport America (107°W, 32°N). The list of rocket launches was obtained from https://en.m.wikipedia.org/wiki/List_of_spaceflight_launches_in_January%E2%80%93June_2022 and https://en.m.wikipedia.org/wiki/List_of_spaceflight_launches_in_July%E2%80%93December_2022.

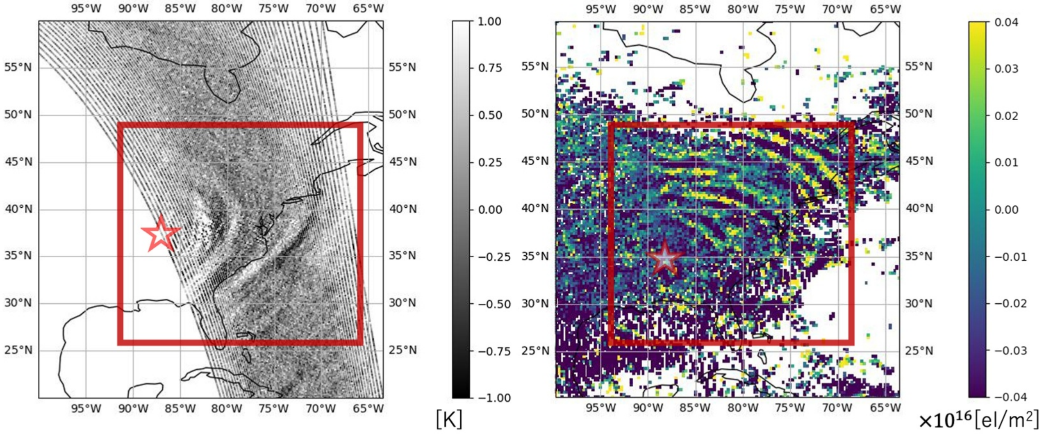

(a) Brightness temperature perturbation 18.24-18.44 UT on June 17, 2022

(b)Total electron content perturbation at 19.56 UT on June 17, 2022

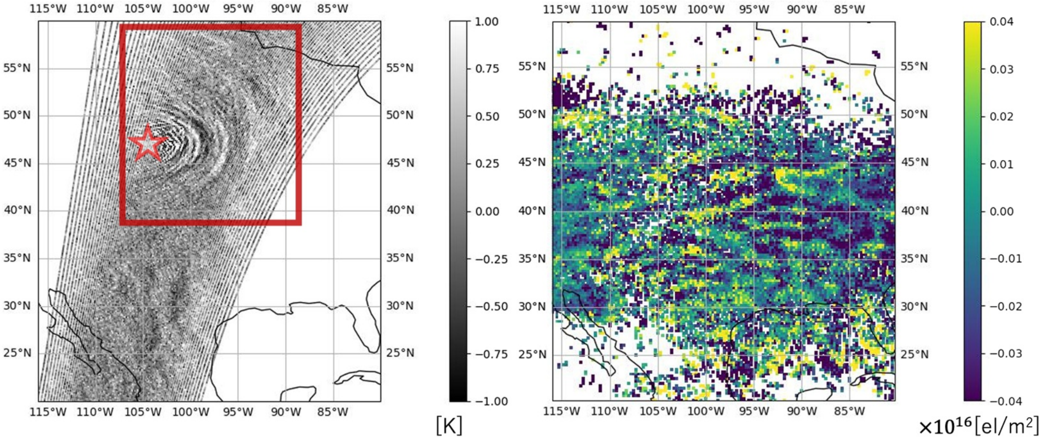

(c) Brightness temperature perturbation 8.83-9.03 UT on July 10, 2022

(d) Total electron content perturbation at 9.37 UT on July 10, 2022

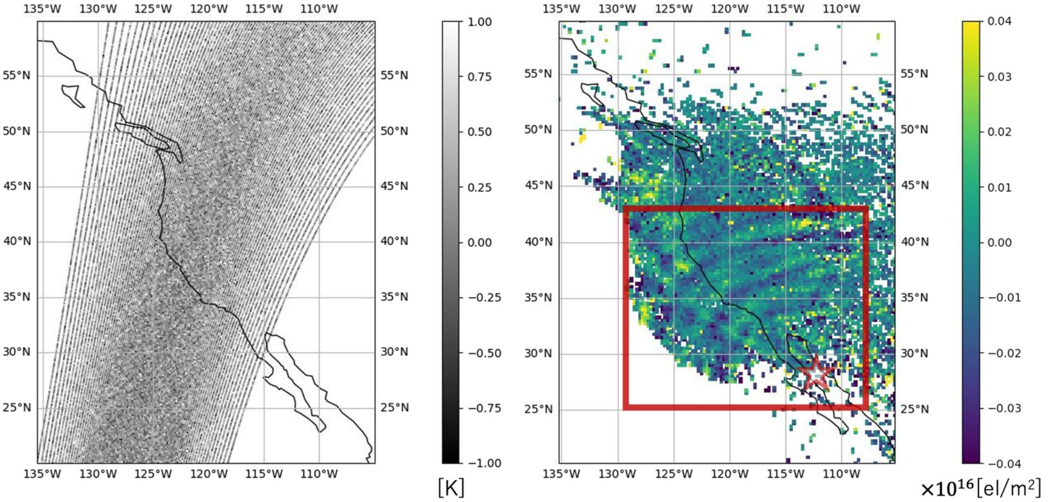

(e) Brightness temperature perturbation 10.15-10.35 UT on September 28, 2022

(f) Total electron content perturbation at 10.07 UT on September 28, 2022

Figure 3. Examples of the simultaneous event in Atmospheric Infrared Sounders (AIRS) and Global Navigation Satellite System Total Electron Content (GNSS-TEC) (a, b) on 17 June 2022, the concentric GW-only event in AIRS (c, d) on 10 July 2022, and the concentric TID-only event in GNSS-TEC on 28 September 2022 (e, f). The red rectangles indicate concentric gravity waves (GWs)/concentric traveling ionospheric disturbances (TIDs). The stars indicate the epicenters of concentric GWs/concentric TIDs.

4. Result: Distribution of Epicenters of Concentric GWs and Concentric TIDs

Figure 4 shows the distributions of the epicenters for the simultaneous GW and TID cases (a–d) and the GW-only cases in AIRS (e–h) across the four seasons. As there was frequently a distance of a few degrees between the epicenters of GWs and TIDs, the location of the GWs' epicenter was chosen to represent the epicenter of TIDs because the stratosphere is closer to the GW sources in the troposphere. The orange and black circles represent epicenters during daytime and nighttime, respectively. Table 1 shows the occurrence numbers and rate for the simultaneous and GW-only cases in each season during daytime and nighttime. TID-only in GNSS-TEC cases and the three types in AIM are shown in Figures S3–S5 in Supporting Information S1. It should be noted that the occurrence number and rate of TID-only cases (287 cases in total, including daytime and nighttime, corresponding to a 40% occurrence rate) were approximately twice as high as those of simultaneous cases. However, this higher occurrence rate might result from the narrower temporal and geographical coverage of AIRS compared to the ground-based GNSS-TEC observations. The number and rate of simultaneous cases in Table 1 were highest in summer (69 cases in total and 38% on average) and clustered over the central U.S. and the Gulf of Mexico (~80–100°W, 25–50°N) in Figure 4c. This cluster can be seen in spring, although the occurrence number and rate were smaller than in summer (20 cases in total and 12% on average). This result is consistent with Hoffmann and Alexander (2010), who reported that the Great Plains (~30–45°N, 80–100°W) is a hot spot of stratospheric GWs generated by thunderstorms. On the other hand, the simultaneous cases in winter (26 cases in total and 15% on average) were clustered between 40 and 50°N and did not appear south of 35°N. In fall, the occurrence number was the smallest (13 cases in total and 7% on average), and the epicenters appeared over ~28–52°N, 65–82°W and ~32–48°N, 102–115°W. This seasonal variation cannot be attributed to contamination from Joule heating-driven TIDs, which obscures concentric TIDs, because the occurrence rate of high Kp index events was comparable each season. These geographical and seasonal variations seem to be attributed to the source activity of GWs driving the TIDs, which will be discussed in Section 5.

Although the occurrence of the GW-only cases is generally smaller than that of the simultaneous GWs and TIDs cases, except in fall, the geographical distributions are similar. The similar geographical distributions can be found in TID-only cases as well, although TID-only events can be seen frequently over the Pacific Ocean, where GW-only and simultaneous events did not appear (See Figure S2 in Supporting Information S1). The epicenters in summer and fall were clustered in the low latitudes, while those from fall to spring were clustered in high latitudes. These similarities suggest that the primary sources of the GW-only cases were the same as those of the simultaneous cases, with GWs potentially being filtered out by background winds above an altitude of ~40 km. Another possible mechanism for non-concentric TIDs in GNSS-TEC is that reduced electron density during nighttime, compared to daytime, weakens the amplitudes of TIDs, obscuring concentric TIDs. Additionally, contamination from Perkins instability-type TIDs could obscure GW-type TIDs during nighttime. Indeed, the total number and ratio of GW-only events during nighttime (44 events and 12%) is larger than that during daytime (23 events and 6%), although it is vice versa for simultaneous events. However, there are also differences between GW-only and simultaneous cases. For example, the clustered epicenters in the low latitudes in spring, which appear in Figure 4b, are not visible in Figure 4f. Although we will compare the distribution of the epicenters with the background wind in Section 6, background wind filtering cannot account for the difference between GW-only and simultaneous ceases. This difference might be attributed to variations in the GW source spectra; however, addressing this is beyond the scope of our paper.

Regarding local time variation, the epicenters of simultaneous cases in winter and fall (Figures 4a and 4d) during daytime (orange double circle) were present at ≥~42°N, while those during nighttime (black double circle) were present at ≤~42°N. This geographical pattern is not observed in Figures 4e and 4h. The total occurrence numbers across all seasons also have a clear local time variation. Specifically, the number of simultaneous cases during daytime was 1.5 times larger than that during nighttime (Table 1). In contrast, the number of GW-only cases during daytime was two times less than that during nighttime. This trend is consistent across all seasons except for fall. The trend of simultaneous and GW-only events might be attributed to a local time variation of stratospheric GW activities. Hoffmann and Alexander (2010) analyzed the AIRS 4 μm data set over the continental U.S. during a thunderstorm season (May to August) and found that stratospheric GW activity was higher in nighttime than in daytime. Indeed, in fall, the total occurrence of concentric GWs in the stratosphere (simultaneous + GW-only events) was higher during nighttime (20 events) than during daytime (15 events). However, in the other seasons, the total occurrence was either the same or lower during nighttime than during daytime. This result differs from Hoffmann and Alexander (2010), but this discrepancy might be attributed to a different sensibility to GW spectra

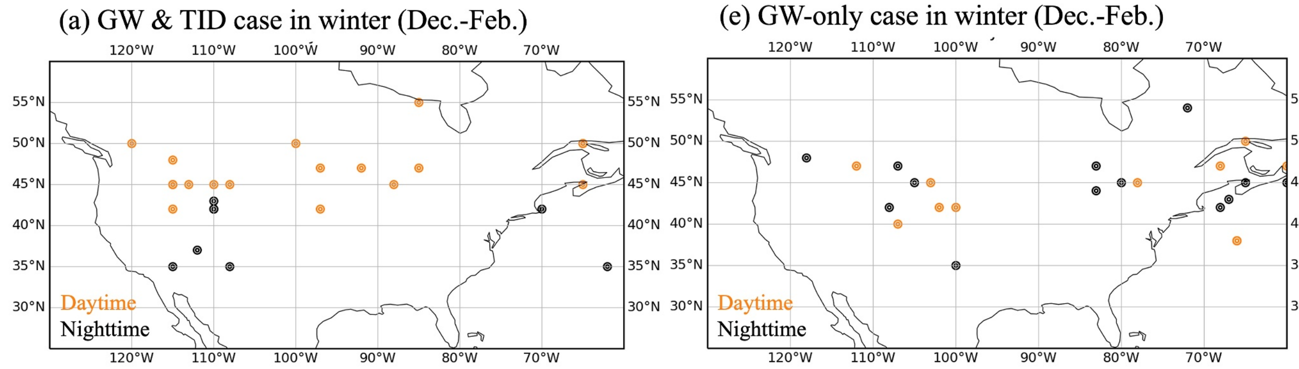
(a) GW & TID case in winter (Dec.-Feb.)

(e) GW-only case in winter (Dec.-Feb.)

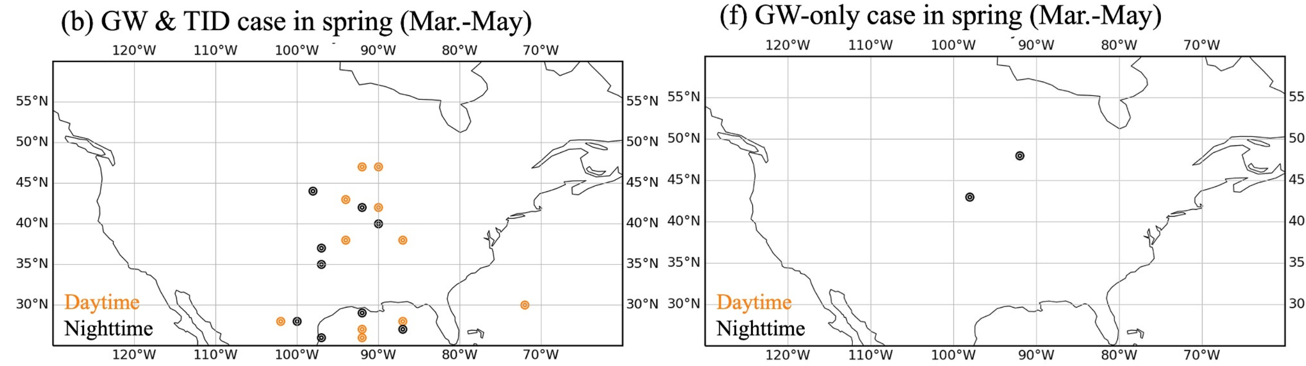
(b) GW & TID case in spring (Mar.-May)

(f) GW-only case in spring (Mar.-May)

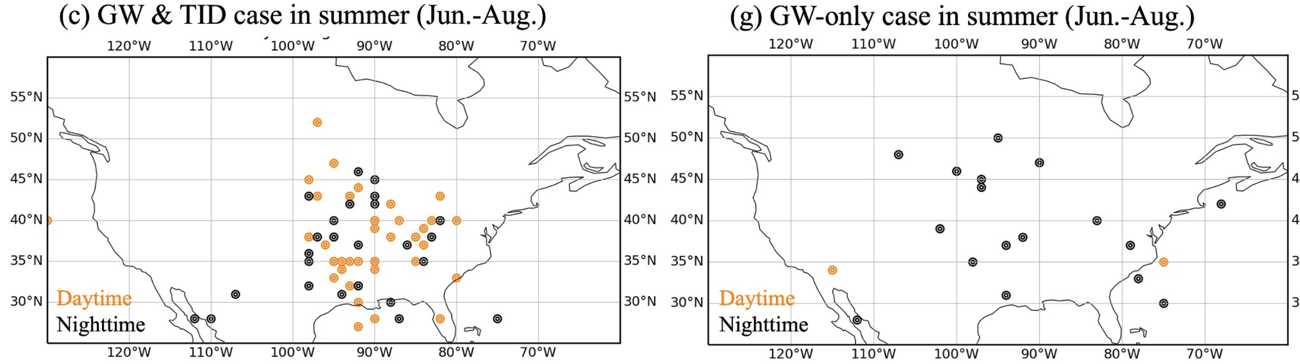
(c) GW & TID case in summer (Jun.-Aug.)

(g) GW-only case in summer (Jun.-Aug.)

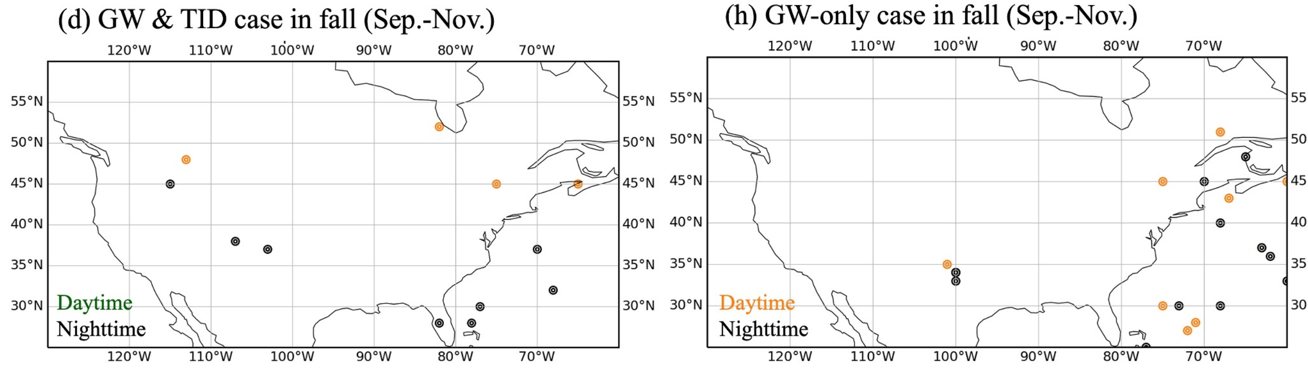
(d) GW & TID case in fall (Sep.-Nov.)

(h) GW-only case in fall (Sep.-Nov.)

Figure 4. Distributions of simultaneous concentric GWs and concentric TIDs in winter (a), spring (b), summer (c), and fall (d). (e–h) Are the same as (a–d), respectively, but for the GW-only case. The orange and black double circles indicate epicenters of concentric GWs and concentric TIDs during daytime and nighttime, respectively.

between the 4 and 15 μm data. Thus, the general local time variation is possibly attributed to the occurrence of concentric TIDs rather than GW source activity. These local time variations could be explained by the local time variation in the thermospheric wind direction, which will be discussed in Section 6.

Table 1
Occurrence Numbers of the Simultaneous Cases and GW-Only Cases During Daytime and Nighttime for Each Season

Season	Local time	GWs and TIDs	GWs	(GWs and TIDs)/(GWs and TIDs + GWs) [%]
Winter	daytime	18 (21%)	11 (13%)	62
	nighttime	8 (9%)	13 (15%)	38
Spring	daytime	11 (13%)	0 (0%)	100
	nighttime	9 (11%)	2 (2%)	82
Summer	daytime	42 (46%)	2 (2%)	95
	nighttime	27 (29%)	17 (18%)	61
Fall	daytime	5 (5%)	10 (11%)	33
	nighttime	8 (9%)	12 (6%)	40
Total	daytime	76 (21%)	23 (6%)	77
	nighttime	52 (15%)	44 (12%)	54
	day + nighttime	128 (18%)	67 (9%)	66

Note. The numbers in parentheses indicate occurrence rates (the occurrence numbers divided by the number of available dates).

Finally, concentric TIDs appear in 66% of the total stratospheric GW events (the number of simultaneous + only-GW cases). In particular, the TID occurrence rate reaches 77% during daytime, although the rate is ~30% in fall. This result suggests that more than half of the concentric GWs in the stratosphere propagate directly to the thermosphere/ionosphere or breaking of the convectively-generated concentric GWs induces secondary GWs with concentric fronts, driving the concentric TIDs, above the stratopause (Heale, Inchin, & Snively, 2022).

5. Potential Meteorology Sources of Concentric GWs and Concentric TIDs

As far as we know, the main sources of concentric GWs and concentric TIDs are Tsunami associated with earthquakes, convection, and the breaking of GWs, that is, secondary generation (Galvan et al., 2012; Heale, Bossert, & Vadas, 2022; Heale, Inchin, & Snively, 2022; Heale et al., 2014; Hickey et al., 2009; Kogure et al., 2020; Liu et al., 2014; Vadas & Azeem, 2021; Vadas & Fritts, 2004, 2005, 2006; Vadas & Liu, 2009). Because there was no epicenter of significant tsunami around the continental U.S. in 2022 (https://www.ncei.noaa.gov/products/natural-hazards/tsunamis-earthquakes-volcanoes/tsunamis/recent-significant-events), a tsunami can be excluded as a potential source. The GWs captured by AIRS are primarily generated by convection rather than the secondary generation mechanism, then propagate directly into the thermosphere/ionosphere or break above the stratopause, producing secondary/tertiary GWs with concentric fronts. Becker and Vadas (2018) and Vadas and Becker (2019) show that secondary GWs with large amplitudes are often generated above the stratosphere, which is higher than the AIRS observation height (~40 km). Also, secondary/tertiary GW have smaller amplitudes when their primary GWs break at lower altitudes (Becker et al., 2022; Vadas & Becker, 2019). Thus, convection is likely the primary source of stratospheric GWs and the GWs driving concentric TIDs.

We used the 8 μm brightness temperature observed by the AIRS data set to examine the correlation between deep convection and concentric TIDs associated with stratospheric GWs in accordance with Hoffmann and Alexander (2010). We define a brightness temperature of less than 220 K as a signal of deep convection clouds, following Hoffmann and Alexander (2010), and collect such events on a 1° × 1° longitude-latitude grid. Figure 5 shows a geographical distribution of the occurrence numbers of deep convection in each season, superimposed with the epicenters of simultaneous concentric GWs and concentric TIDs. Most epicenters are located within ~2–3° distance of deep convection, though some (four events in ~20–23°N, ~86–92°W in spring, and two events in ~33–34°N, ~102–106°W) are as far as ~5° away. Specifically, the clustered epicenters over the central U.S. (~80–100°W, 25–50°N) obviously correspond to the deep convection during spring and summer, which is consistent with Hoffmann and Alexander (2010). Deep convection occurred between 30 and 50°N aligns with the clustered epicenters, suggesting it is the most likely source of GWs driving concentric TIDs over the continental U.S. throughout all seasons.

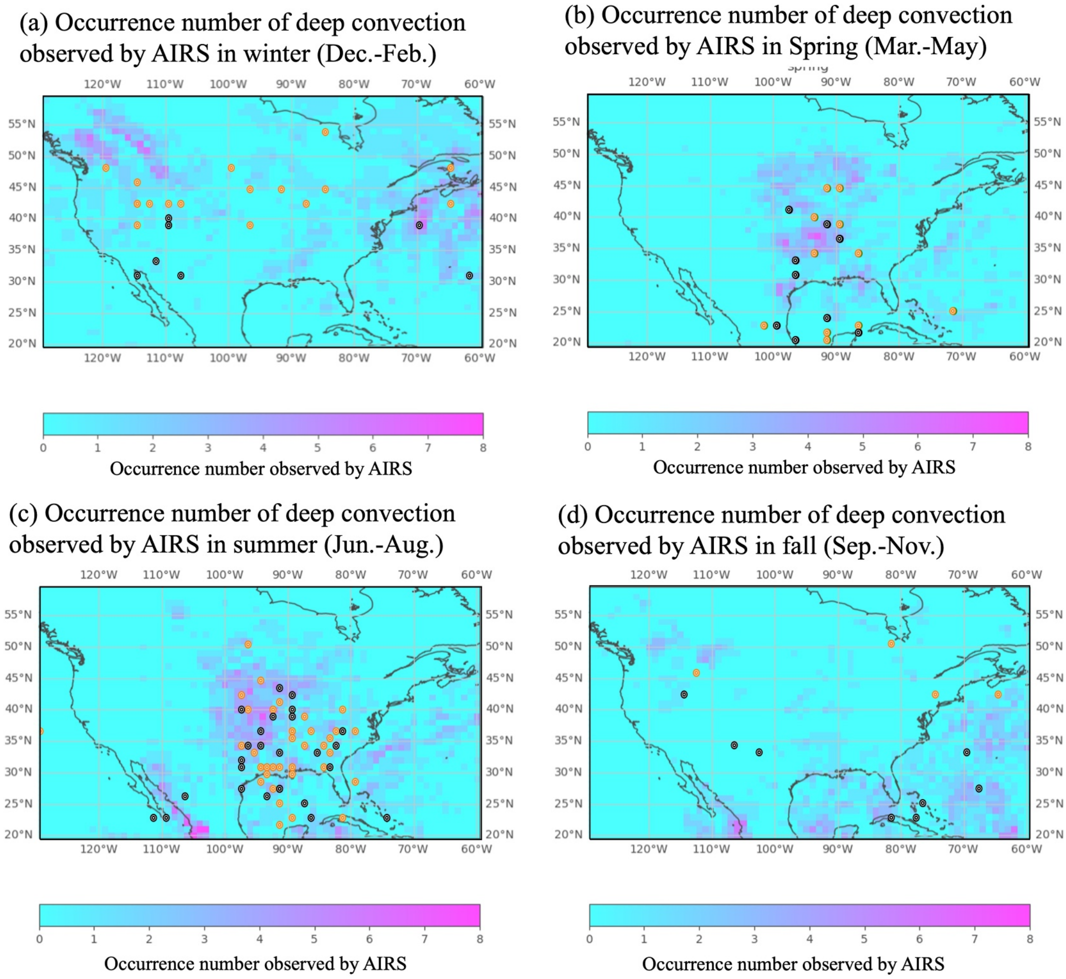

Figure 5. Geographical distributions of the occurrence numbers of deep convection in winter (a), spring (b), summer (c), and fall (d). The orange and black double circles are the same as in Figures 4a–4d.

To further investigate metrological phenomena associated with deep convection, we analyze the North American Mesoscale Forecast System (NAM) analysis (Colbert et al., 2019). Convection typically occurs in regions with high convective available potential energy (CAPE) (Holton & Hakim, 2013) or within extratropical cyclones (Evans, 2010; Uccelini, 1990; Wernli et al., 2002).

Figure 6 shows the seasonal mean CAPE obtained from the NAM analysis (Colbert et al., 2019). CAPE is defined as the maximum possible upward kinetic energy per unit mass that a buoyant parcel can obtain from the free convection level to the neutral buoyancy level (Holton & Hakim, 2013). CAPE values, which indicate the potential for strong convection, are generally high around the Gulf of California (~108–115°W, 25–30°N), the Gulf of Mexico (~85–95°W, 25–30°N), and the North Atlantic Ocean (~60–80°W, 25–40°N). The area with a seasonal mean CAPE higher than 400 J kg^{-1} area (white-to-red area in Figure 5) was largest in summer (Figure 6c), corresponding to the cluster of the GW's and TID's epicenters (~80–100°W, ~25–45°N) in Figure 4c. Similarly, the area around the Gulf of Mexico and the North Atlantic Ocean in spring corresponds to the region with a seasonal mean CAPE higher than 400 J kg^{-1}, and the clustered epicenters can be seen there (Figure 4b), although the CAPE values and the number of the epicenters were lower in spring than in summer. Changnon and Changnon (2001) showed the climatological number of thunderstorm days and the high number in ~80–100°W, ~25–45°N, where the CAPE and the deep convection and concentric GWs' and TIDs' occurrence rates were high. Hoffmann and Alexander (2010) also showed that this region is a hot spot of stratospheric GW associated with deep convection in a thunderstorm season (May to August). Therefore, the potential source of the GWs driving the concentric TIDs was convection within thunderstorms. In fall, four epicenters in Figure 4d appeared over the

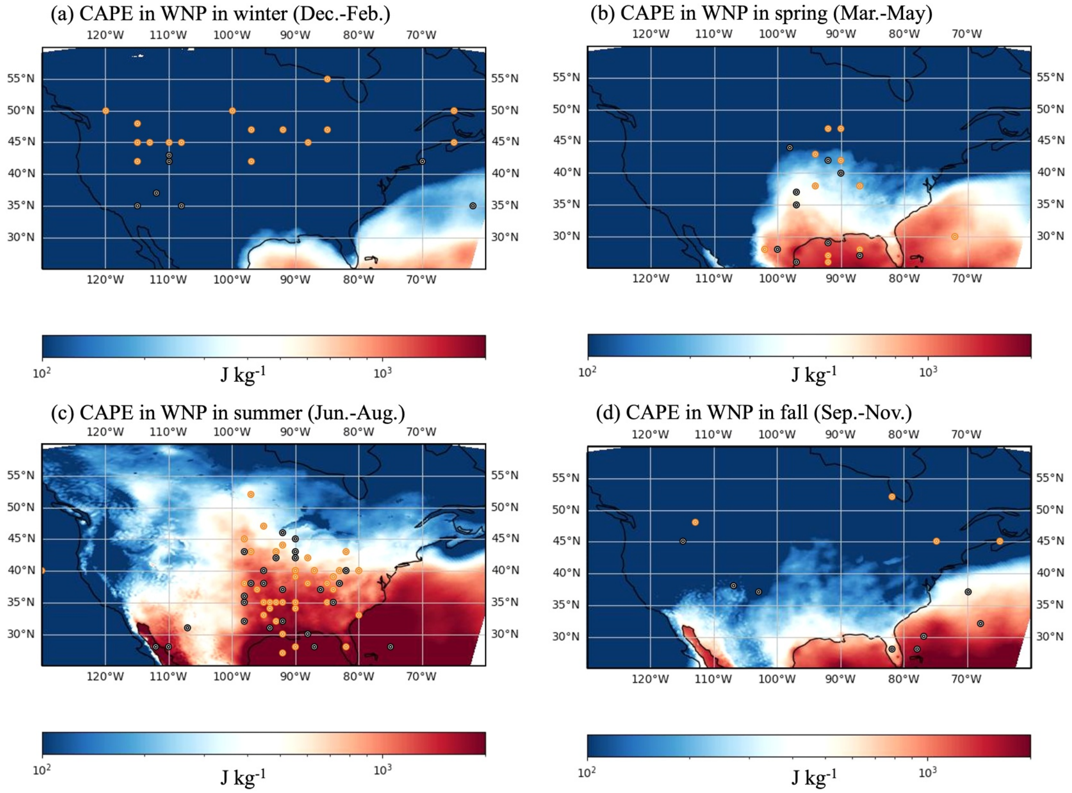
(a) CAPE in WNP in winter (Dec.-Feb.)
(b) CAPE in WNP in spring (Mar.-May)
(c) CAPE in WNP in summer (Jun.-Aug.)
(d) CAPE in WNP in fall (Sep.-Nov.)

Figure 6. (a) Convective available potential energy (CAPE) averaged in winter 2022 (January, February, and December). The CAPE values were obtained from the North American Mesoscale Forecast System (NAM) analysis. (b–d) are the same as (a) but for spring (March to May), summer (June to August), and fall (September to November), respectively. The orange and black double circles are the same as in Figures 4a–4d.

North Atlantic Ocean south of 40°N, where the CAPE values were high. Their potential source was also convection. Given that the North Atlantic Ocean during fall is well known for tracks of tropical cyclones, that is, Hurricanes (Landsea, 1993), some of the convection could be associated with Hurricanes rather than thunderstorms. We compared the timing of the GW-only and simultaneous events with Hurricanes in 2022 (https://www.nhc.noaa.gov/data/tcr/index.php?season=2022&basin=atl). One GW-only and two simultaneous events occurred over Hurricane Nicole during 9–11 November.

However, the distribution of TID's epicenters does not align with CAPE values over the continental U.S. in winter and northern U.S. (north of ∼35°N) in spring and fall. The epicenters were clustered in 35–50°N, and their activity was higher in winter than those in spring and fall. These features are consistent with the characteristics of extratropical cyclones, suggesting that their potential source is convection within extratropical cyclones. Large-scale vertical motions within extratropical cyclones are driven by horizontal temperature gradients, that is, baroclinic force (subsection 9.2.3. in Holton & Hakim, 2013). The large-scale motion in a warm and moist air side is upward, inducing latent heating and enforcing small-scale updraft, that is, convection. Because CAPE considers only a vertical temperature profile and neglects the effects of water vapor and condensed water (subsection 9.5.1. in Holton & Hakim, 2013), CAPE may not be a useful index of convective activity within extratropical cyclones. Indeed, previous papers report that convection occurs under low CAPE but high wind shear conditions along cold fronts in fall, winter, and spring (e.g., Burke & Schultz, 2004; Celiński-Mysław & Matuszko, 2014; Celiński-Mysław et al., 2020; Sherburn & Parker, 2014). Since cold fronts appear south of extratropical cyclone's centers, convection under low CAPE conditions occurs preferentially there. Instead of CAPE, we derived the 24-hr difference filtered variance of sea level pressure, called ECApp, from the NAM analysis to measure extratropical cyclone activity and location (Ma & Chang, 2017). ECApp is described in Equation 1 in Ma and Chang. (2017) as the follows:

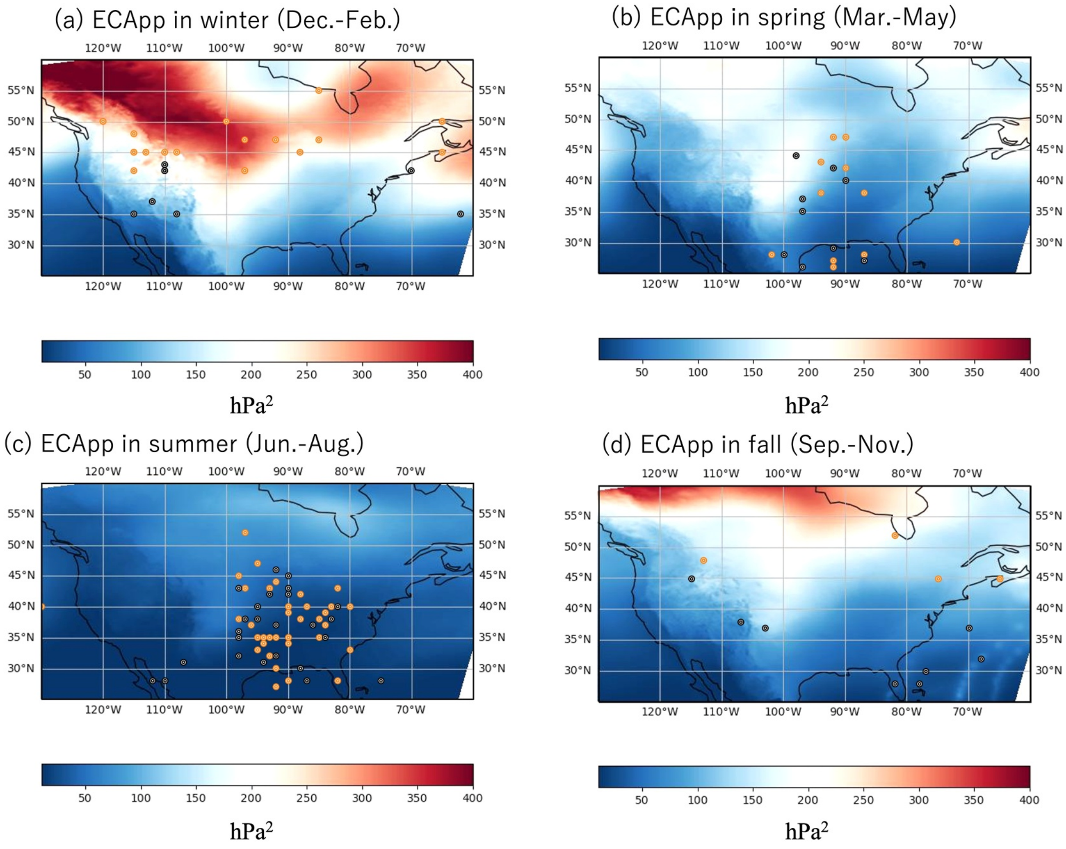

Figure 7. ECApp derived from the NAM analysis in winter (a), spring (b), summer (c), and fall (d). The orange and black double circles are the same as in Figure 4.

$$\mathrm{ECApp} = \overline{\left(P_{s(t+24h)} - P_{s(t)}\right)^2} \tag{1}$$

P_s, t, and $\overline{}$ indicate sea level pressure, time, and seasonal average, respectively. ECApp values become larger with proximity to the center of an extratropical cyclone. It should be noted that anticyclones are slow-moving, and their pressure anomalies are weaker than those of cyclones (Hoskins & Hodges, 2002), so extratropical cyclones predominantly contribute to ECApp (Ma & Chang, 2017). Although ECApp is not a direct index of convection but rather an index of extratropical cyclone activity, convective activity is linked to extratropical cyclone activity. Figure 7 shows the seasonal mean ECApp across the four seasons. The ECApp values generally peak in winter, consistent with the general seasonal variation of extratropical cyclone activity. Also, the geographical distribution of ECApp is in good agreement with its climatology (see Figure 1b in Ma & Chang, 2017); that is, the values are roughly higher in high latitudes than in low latitudes. It should be noted that a few white lines can be seen in the North Atlantic Ocean in fall. These lines correspond to tracks of centers of Hurricanes, Earl and Fiona, not centers of extratropical cyclones. However, any epicenter was not found over the North Atlantic Ocean when both Hurricanes passed over there. Although the epicenters of the concentric TIDs north of ~35°N were relatively closer to ECApp values higher than 200 hPa^2, the epicenters appeared in ~2–15° south of the local maximum ECApp. For example, the ECApp values peaked at 105–115°W, 50°N in winter (Figure 7a), while the epicenters were clustered around 105–115°W, 35–48°N (Figure 4a). This southern preference is possibly natural because a cold front, where convection preferentially occurs despite low CAPE values, appears south of an extratropical cyclone's center. In addition, warm and moist air, where upward motion and convection occur, is located south of the center of an extratropical cyclone in the sea level pressure, which corresponds to a high ECApp area. Upward motion and convection are induced in warm and moist air, so epicenters of convectively-generated GWs could prefer to appear a few to several degrees south of an extratropical cyclone's center Figure 7.

To summarize the potential sources of GWs driving concentric TIDs, it is likely convection over the entire continental U.S. and all seasons. However, weather phenomena associated with convection could vary by season and latitude. The convection could be associated with thunderstorms over the central-eastern U.S. in summer and the southern U.S. in spring, while it could be associated with extratropical cyclones over the northern U.S. during winter, spring, and fall. The convection over the North Atlantic Ocean in fall could be associated with hurricanes.

6. Background Wind Effect on Concentric GWs and Concentric TIDs

The simultaneous cases show local time variations, but the stratospheric GW occurrences (total of GW-only plus simultaneous events) do not exhibit such variations. This result suggests that local time variations in concentric TIDs are caused by changes in the background wind above ~40 km altitude. Another possible mechanism is the higher background electron density during daytime compared to nighttime. Hooke (1968) demonstrated that the amplitudes of TIDs driven by GWs are proportional to background electron density. It is well known that background electron density is higher during daytime than during nighttime. Otherwise, Perkins instability-type TIDs obscure GW-type TIDs during nighttime because the former TIDs generally have larger amplitudes than the latter ones. Here, we focus on the background wind effect on the local time variation of TIDs.

Figure 8 shows vertical profiles of the seasonal mean zonal and meridional winds, averaged over 60–130°W at 25, 37, and 50°N at specific local times, obtained from the SD-WACCM-X model (Specified Dynamics Whole Atmosphere Community Climate Model with thermosphere and ionosphere eXtension) (Liu et al., 2018; Sassi et al., 2013). This SD-WACCM-X simulation below ~50 km altitude is nudged with MERRA-2 (The Modern-Era Retrospective Analysis for Research and Applications, Version 2) (Gelaro et al., 2017). The longitudinal, latitudinal, and temporal resolutions of the output data are 1.25°, 0.9°, and 1 hr, respectively. The two local times are chosen as the time closest to when AIRS passes through each longitude, that is, ~1.5 LT (a–c, g–i) and ~13.5 LT (d–f, j–l). As expected, local time variations in zonal and meridional winds above ~120 km were quite significant in all seasons and latitudes (up to ~250 ms^{-1} for the meridional wind at 50°N in summer), while variations below ~120 km were smaller. The magnitudes of the zonal and meridional winds above ~120 km were larger at nighttime (Figure 8a–8c, 8g–8i) than those during daytime (Figure 8d–8f, 8j–8l), especially in summer. For example, the nighttime westward and southward winds in summer exceeded ~100 and 200 ms^{-1}, respectively, at 50°N, while the daytime winds were ~30 ms^{-1}. This weaker daytime wind is attributed to stronger ion drag from solar radiation and ionization. Heale, Inchin, and Snively (2022) simulated primary and secondary GWs emitted from squall lines, showing that the phase speed ranges of primary and secondary GWs are 170–320 ms^{-1} and ~100–600 ms^{-1} in the thermosphere. According to a simulation conducted by Vadas and Crowley (2010), phase speed spectra of secondary GWs, whose primary GWs were induced by equatorial convection, peak in the range of ~100–300 ms^{-1}. Assuming that TIDs' phase speeds are in the range of ~100–300 ms^{-1}, the nighttime wind exceeding 100 ms^{-1} potentially filtered out some parts of TIDs. During daytime, the weaker wind speed in the thermosphere enables GWs to propagate through the thermosphere/ionosphere, increasing (decreasing) the occurrence number of simultaneous (GW-only) cases. On the other hand, the stronger nighttime wind could filter out or distort concentric GWs, increasing (decreasing) the occurrence number of GW-only (simultaneous) cases.

The local time variation of the thermospheric wind could also induce the local time and latitudinal variations of the simultaneous cases in fall and winter; that is, those cases were present at ≥~42°N during daytime and ≤~42°N during nighttime (see Figure 4a). The northward wind during the daytime (Figure 8l) suggests that southward-propagating GWs were dominant. Considering the dense receiver area between 30 and 50°N, GNSS-TEC possibly tends to capture the south sides of concentric rings with their epicenters at high latitudes. On the other hand, the southward wind at nighttime (Figure 8i) could suppress southward-propagating GWs, resulting in the preference occurrence south of ~42°N. It should be noted that the background wind drastically controls dissipation on GWs, even if their phase speed is much higher than the background wind speed (Fritts & Vadas, 2008; Vadas, 2007). In addition to the dissipation, GNSS-TEC receivers can detect TIDs only with vertical wavelengths exceeding ~100 km, as they observe electron content integrated vertically. Alexander et al. (2011) describes the relationship between a vertical wavelength and background wind under the midfrequency approximation as follows:

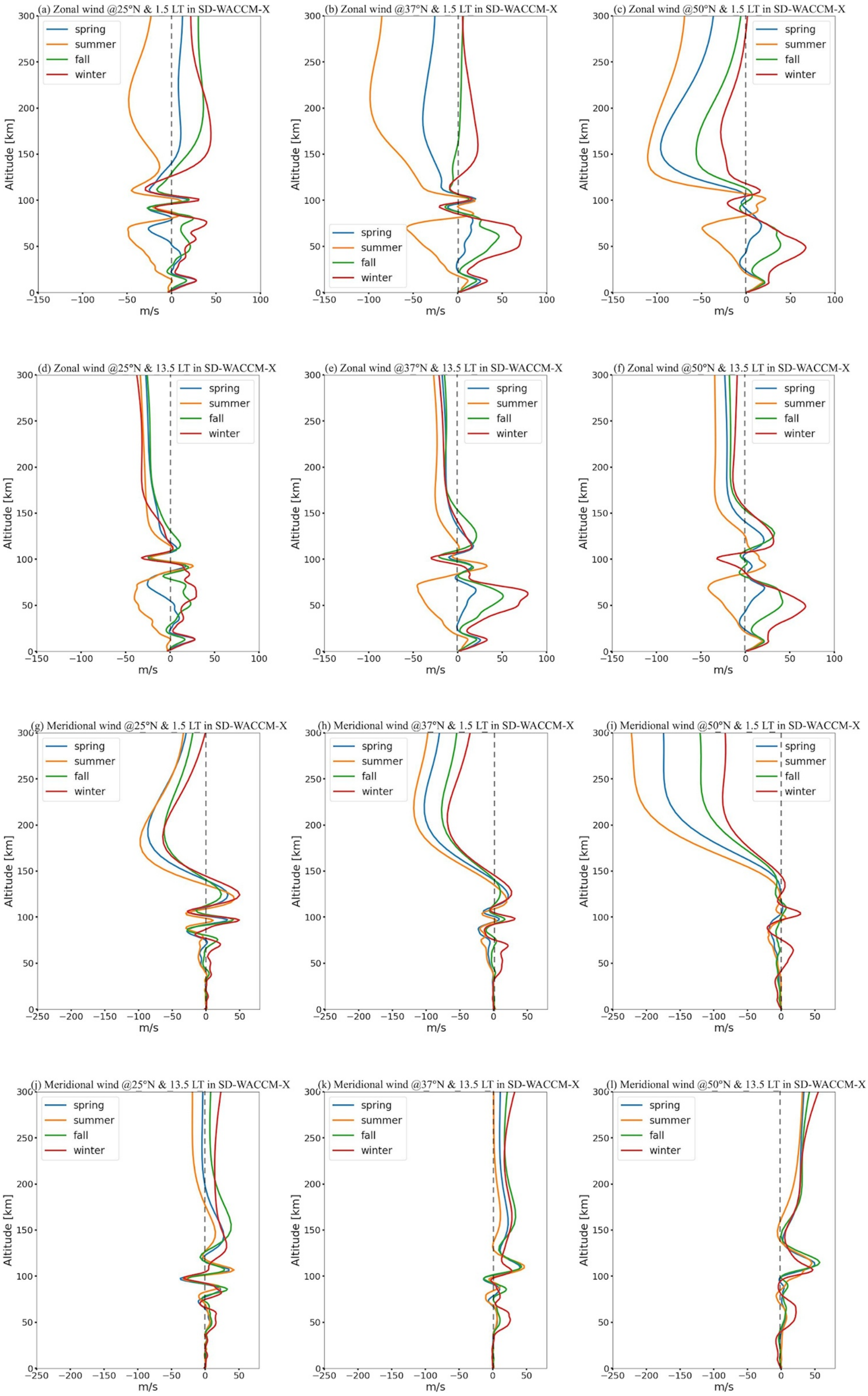

Figure 8. (a–c) Vertical wind profiles of the seasonal mean zonal wind at ~1.5 LT averaged over 60–130°W at 25°, 37°, and 50°N, respectively, in SD-WACCM-X. (d–f) Same as (a–c), respectively, but for the meridional wind. (g–l) Same as (a–f), but at ~13.5 LT.

Table 2
Summary of Regions of Clustered Epicenter and Specific Weather Phenomena Associated With Convection for Each Season

Season	Region of clustered epicenter	Specific weather phenomena associated with convection
Winter	North of ~40°N	Extratropical cyclones
Spring	South of ~40°N	Thunderstorms
	North of ~40°N	Extratropical cyclones
Summer	Central-to-eastern U.S. (~80–100°W, 25–50°N)	Thunderstorms
Fall	South of ~40°N	Thunderstorms and tropical cyclone
	North of ~40°N	Extratropical cyclones

$$\lambda_{z(z)} = \frac{2\pi}{N_{(z)}}\left(c_h - \overline{u}_{h(z)}\right), \tag{2}$$

where $\lambda_{z(z)}$, $N_{(z)}$, c_h, and $\overline{u}_{h(z)}$ represent the vertical wavelength, Brunt–Väisälä frequency, ground-based phase speed, and horizontal wind in the wave propagation direction, respectively. Considering that GNSS-TEC receivers can observe TIDs with vertical wavelengths exceeding ~100 km, the intrinsic phase speed, $c_h - \overline{u}_{h(z)}$, must satisfy the following equation:

$$\left|c_h - \overline{u}_{h(z)}\right| \geq \frac{100\ [\mathrm{km}] \times N_{(z)}}{2\pi}. \tag{3}$$

Given that the typical Brunt–Väisälä frequency at 200–300 km altitudes is $\sim 1.0 \times 10^{-2}\ \mathrm{s}^{-1}$, the minimum observable intrinsic speed is $\sim 160\ \mathrm{ms}^{-1}$. The minimum observable ground-based phase speeds of southward propagating GWs during nighttime are $\sim 270\ \mathrm{ms}^{-1}$ in fall and $\sim 230\ \mathrm{ms}^{-1}$ in winter, while those of northward-propagating are $\sim 50\ \mathrm{ms}^{-1}$ in fall and $\sim 90\ \mathrm{ms}^{-1}$ in winter. Therefore, GNSS-TEC receivers cover the entire range of the typical peak ground-based phase speed spectrum (~ 100–$300\ \mathrm{ms}^{-1}$) of northward propagating GWs and preferentially capture northward propagating GWs during nighttime. Similarly, during daytime, the minimum observable ground-based phase speeds of southward-propagating GWs are $\sim 120\ \mathrm{ms}^{-1}$ in both fall and winter, whereas those of northward-propagating GWs are $\sim 200\ \mathrm{ms}^{-1}$. As a result, GNSS-TEC receivers preferentially capture southward propagating GWs during daytime.

7. Conclusions

We analyzed the seasonal distributions of concentric GWs in the stratosphere and concentric TIDs in the ionosphere in 2022 (a solar medium year) and compared them with weather conditions and background winds in the upper atmosphere. We found that the occurrence number of concentric TIDs associated with stratospheric concentric GWs was highest in summer. Geographical variations in the TID epicenters were consistent with the patterns of deep convection in each season. Table 2 shows a summary of the regions of clustered epicenter and the potential GW sources for each season. Concentric TID epicenters aligned with high CAPE regions over the central-to-eastern U.S. in summer and south of ~40°N in spring and fall. On the other hand, the epicenters in winter and north of ~40°N in spring and fall appeared south of the high EACpp areas, corresponding to centers of extratropical cyclones. Our findings indicate that concentric TIDs associated with stratospheric GWs over the continental U.S. were primarily driven by convection, although the specific weather phenomena varied by season and latitude. These phenomena could be thunderstorms over the central U.S. in summer and the southern U.S. in spring and fall, while those could be extratropical cyclones over the northern U.S. in winter, spring, and fall. Over the North Atlantic during fall, a few events were most likely associated with Hurricane Nicole.

Concentric stratospheric GWs appear to be correlated with concentric TIDs in 66% of all GW events. This suggests that more than half of the convectively-generated GWs directly propagate into the ionosphere, driving concentric TIDs. Convection is one of the primary lower atmospheric sources capable of producing concentric

TIDs in the ionosphere and is therefore an important component of the vertical coupling due to GWs. We also found that the thermospheric wind potentially influences the local time and latitudinal variation of the concentric TIDs associated with stratospheric GWs. Specifically, the thermospheric wind is weaker during daytime than during nighttime, leading to a higher occurrence rate of simultaneous cases during daytime. The higher occurrence rate may also be related to the increased background electron density during daytime. Our results suggest that weather information is highly valuable for understanding atmospheric vertical coupling and predicting TID occurrences.

We focused on the concentric GWs and TIDs in 2022, a moderate solar flux year (F10.7 = 100–150 sfu). Since the kinetic viscosity at a fixed height increases as the thermospheric temperature decreases (due to a concomitant decrease in density), the dissipation of GWs increases with decreasing solar activity (Hickey & Cole, 1981; Otsuka et al., 2021; Vadas, 2007). As a result, the occurrence of concentric TIDs associated with stratospheric GWs may decrease during periods of low solar activity. Conversely, during high solar activity, the opposite trend might occur. On the other hand, a year-to-year variation of GW activity due to convection and background wind should be taken into account since concentric GWs are the driving forces of concentric TIDs. GNSS-TEC data over the continental U.S. and AIRS observations have been available for more than 20 years, allowing us to confirm the effect of solar activity on the occurrence of concentric TIDs in a future study.

This study is the first to statistically examine the correlation between concentric GWs in the stratosphere and concentric TIDs in the ionosphere over the course of a year. Although this paper focuses on simultaneous events, concentric TIDs without concentric GWs in the stratosphere are frequently observed in GNSS-TEC data as well. It is critically important to identify their sources to comprehend the atmospheric vertical coupling. Concentric TIDs without stratospheric GWs may be linked to the secondary GW generation mechanism, possibly related to plain-front GWs in the stratosphere/mesosphere. In addition, the source of their parent waves might be linked to weather phenomena (e.g., jets and flow over mountains). Using a combination of instruments sensitive to different atmospheric layers, as done in this study and previous studies (e.g., de Groot-Hedlin et al., 2017; Kogure, Liu, & Jin, 2023; Kogure, Nakamura, et al., 2023; Kogure et al., 2020; Yue et al., 2013, 2014), could help identify sources of concentric TIDs without concentric GWs in the stratosphere. Our methodology can be applied in low/high latitudes if those regions are widely and densely covered by GPS receivers, similar to the U.S. Since weather phenomena are different between low, middle, and high latitudes, the primary sources of concentric TIDs with concentric GWs in the stratosphere might be different in low/high latitudes from the middle latitudes (the continental U.S.). Also, weather patterns and thermal tides are influenced by large-scale climate phenomena which have interannual variations (e.g., El Niño–Southern Oscillation; Kogure & Liu, 2021; Kogure, Liu, & Jin, 2023; Kogure, Nakamura, et al., 2023; Liu et al., 2017). Those large-scale climate phenomena might influence TID activity, potentially providing insights into the long-term trends of TID activity.

Data Availability Statement

The AIRS gravity wave data sets (Hoffmann, 2021; Hoffmann et al., 2013, 2014, 2017) are provided by Forschungszentrum Jülich (https://datapub.fz-juelich.de/slcs/airs/gravity_waves/data).The AIM gravity wave data set is described by Randall et al. (2017), and is available from the University of Colorado at http://lasp.colorado.edu/aim/download-data-raa.php, as well as the NASA Space Physics Data Facility (SPDF) at https://spdf.gsfc.nasa.gov/pub/data/aim/cips/data/RAA/. The Kp index data sets (Matzka et al., 2021) are provided by Helmholtz-Zentrum Potsdam Deutsches GeoForschungsZentrum (https://kp.gfz-potsdam.de/en/data). The Receiver Independent Exchange Format (RINEX) data used for GNSS-TEC processing were provided by 50 data providers. These have been listed on the webpage of the GNSS-TEC database (http://stdb2.isee.nagoya-u.ac.jp/GPS/GPS-TEC/gnss_provider_list.html). The main contributed providers to the data in this study are UNAVCO, CDDIS, CHAIN, PNGA, SOPAC, RENAG, SONEL, LINZ, TLALOCNET, and NCEDC. The detrended TEC data sets used in this study (Kogure & Otsuka, 2025a, 2025b, 2025c, 2025d, 2025e, 2025f) can be accessed through the following links. January and February: https://doi.org/10.5281/zenodo.14625201. March and April: https://zenodo.org/records/14625725. May and June: https://zenodo.org/records/14625733. July and August: https://zenodo.org/records/14625750. September and October: https://zenodo.org/records/14625756. November and December: https://zenodo.org/records/14625777.

Acknowledgments

MK was supported by JSPS KAKENHI Grants JP23K13160, 22KJ2409, and 22J00331. HL acknowledges support by JSPS Grant JP22K21345. CER acknowledges support from NASA Grant 80NSSC20K0628. This research was supported by Global—Learning & Academic research institution for Master's·PhD students, and Postdocs Program of the National Research Foundation of Korea(NRF) grant funded by the Ministry of Education (No. RS-2024-00442483).

References

Afraimovich, E. L., Kosogorov, E. A., & Plotnikov, A. V. (2002). Shock-acoustic waves generated during rocket launches and earthquakes. *Cosmic Research*, *40*(3), 241–254. https://doi.org/10.1023/A:1015925020387

Alexander, S. P., Klekociuk, A. R., & Murphy, D. J. (2011). Rayleigh lidar observations of gravity wave activity in the winter upper stratosphere and lower mesosphere above Davis, Antarctica (69°S, 78°E). *Journal of Geophysical Research*, *116*(D13), D13109. https://doi.org/10.1029/2010JD015164

Arendt, P. R. (1971). Ionospheric undulations following Apollo 14 launching. *Nature*, *231*(438), 438–439. https://doi.org/10.1038/231438a0

Aumann, H. H., & Pagano, T. S. (2003). Early results from AIRS on the EOS. In *Proceedings of SPIE 4881, Sensors, Systems, and Next-Generation Satellites VI*. https://doi.org/10.1117/12.462605

Azeem, I., & Barlage, M. (2018). Atmosphere-ionosphere coupling from convectively generated gravity waves. *Advances in Space Research*, *61*(7), 1931–1941. https://doi.org/10.1016/j.asr.2017.09.029

Azeem, I., Vadas, S. L., Crowley, G., & Makela, J. J. (2017). Traveling ionospheric disturbances over the United States induced by gravity waves from the 2011 Tohoku tsunami and comparison with gravity wave dissipative theory. *Journal of Geophysical Research: Space Physics*, *122*(3), 3430–3447. https://doi.org/10.1002/2016JA023659

Bailey, S. M., Thomas, G. E., Rusch, D. W., Merkel, A. W., Jeppesen, C. D., Carstens, J. N., et al. (2009). Phase functions of polar mesospheric cloud ice as observed by the CIPS instrument on the AIM satellite. *Journal of Atmospheric and Solar-Terrestrial Physics*, *71*(3–4), 373–380. https://doi.org/10.1016/j.jastp.2008.09.039

Becker, E., Goncharenko, L., Harvey, V. L., & Vadas, S. L. (2022). Multi-step vertical coupling during the January 2017 sudden stratospheric warming. *Journal of Geophysical Research: Space Physics*, *127*(12), e2022JA030866. https://doi.org/10.1029/2022JA030866

Becker, E., & Vadas, S. L. (2018). Secondary gravity waves in the winter mesosphere: Results from a high-resolution global circulation model. *Journal of Geophysical Reseach: Atmospheres*, *123*(5), 2605–2627. https://doi.org/10.1002/2017JD027460

Bowling, T., Calais, E., & Haase, J. S. (2013). Detection and modeling of the ionospheric perturbation caused by a space shuttle launch using a network of ground-based Global Positioning System stations. *Geophysical Journal International*, *192*(3), 1324–1331. https://doi.org/10.1093/gji/ggs101

Bristow, W. A., Greenwald, R. A., & Samson, J. C. (1994). Identification of high-latitude acoustic gravity wave sources using the loose bay HF radar. *Journal of Geophysical Research*, *99*(A1), 319–331. https://doi.org/10.1029/93JA01470

Burke, P. C., & Schultz, D. M. (2004). A 4-yr climatology of cold-season bow echoes over the continental United States. *Weather and Forecasting*, *19*(6), 1061–1074. https://doi.org/10.1175/811.1

Calais, E., & Minster, J. N. (1996). GPS detection of ionospheric perturbations following a space shuttle ascent. *Geophysical Research Letters*, *23*(15), 1897–1900. https://doi.org/10.1029/96GL01256

Carstens, J. N., Bailey, S. M., Lumpe, J. D., & Randall, C. E. (2013). Understanding uncertainties in the retrieval of polar mesospheric clouds from the cloud imaging and particle size experiment in the presence of a bright Rayleigh background. *Journal of Atmospheric and Solar-Terrestrial Physics*, *104*, 197–212. https://doi.org/10.1016/j.jastp.2013.08.006

Celiński-Mysław, D., & Matuszko, D. (2014). An analysis of the selected cases of derecho in Poland. *Atmospheric Research*, *149*, 263–281. https://doi.org/10.1016/j.atmosres.2014.06.016

Celiński-Mysław, D., Palarz, A., & Taszarek, M. (2020). Climatology and atmospheric conditions associated with cool season bow echo storms in Poland. *Atmospheric Research*, *240*, 104944. https://doi.org/10.1016/j.atmosres.2020.104944

Chahine, M. T., Pagano, T. S., Aumann, H. H., Atlas, R., Barnet, C., Blaisdell, J., et al. (2006). AIRS: Improving weather forecasting and providing new data on greenhouse gases. *Bulletin of the American Meteorological Society*, *87*(7), 911–926. https://doi.org/10.1175/BAMS-87-7-911

Changnon, S. A., & Changnon, D. (2001). Long-term fluctuations in thunderstorm activity in the United States. *Climatic Change*, *50*(4), 489–503. https://doi.org/10.1023/A:1010651512934

Chimonas, G., & Hines, C. O. (1969). Atmospheric gravity waves launched by auroral currents. *Planetary and Space Science*, *18*(4), 565–582. https://doi.org/10.1016/0032-0633(70)90132-7

Chou, M.-Y., Lin, C. C. H., Shen, M.-H., Yue, J., Huba, J. D., & Chen, C.-H. (2018). Ionospheric disturbances triggered by SpaceX falcon heavy. *Geophysical Research Letters*, *45*(13), 6334–6342. https://doi.org/10.1029/2018GL078088

Chou, M. Y., Lin, C. C. H., Yue, J., Tsai, H. F., Sun, Y. Y., Liu, J. Y., & Chen, C. H. (2016). Concentric traveling ionosphere disturbances triggered by Super Typhoon Meranti. *Geophysical Research Letters*, *44*(3), 1219–1226. https://doi.org/10.1002/2016GL072205

Clark, T. L., Hauf, T., & Kuettner, J. P. (1986). Convectively forced internal gravity waves: Results from two-dimensional numerical experiments. *Quarterly Journal of the Royal Meteorological Society*, *112*(474), 899–925. https://doi.org/10.1002/qj.49711247402

Colbert, M., Stensrud, D. J., Markowski, P. M., & Richardson, Y. P. (2019). Processes associated with convection initiation in the North American mesoscale forecast system, version 3 (NAMv3). *Weather and Forecasting*, *34*, 683–700. https://doi.org/10.1175/WAF-D-18-0175.1

Cowling, D. H., Webb, H. D., & Yeh, K. C. (1971). Group rays of internal gravity waves in a wind-stratified atmosphere. *Journal of Geophysical Research*, *76*(1), 213–220. https://doi.org/10.1029/JA076i001p00213

Crowley, G., Jones, T. B., & Dudeney, J. R. (1987). Comparison of short period TID morphologies in Antarctica during geomagnetically quiet and active intervals. *Journal of Atmospheric and Terrestrial Physics*, *49*(11–12), 1155–1162. https://doi.org/10.1016/0021-9169(87)90098-5

Crowley, G., & Rodrigues, F. S. (2012). Characteristics of traveling ionospheric disturbances observed by the TIDDBIT sounder. *Radio Science*, *47*(04), 1–12. https://doi.org/10.1029/2011RS004959

de Groot-Hedlin, C. D., Hedlin, M. A. H., Hoffmann, L., Alexander, M. J., & Stephan, C. C. (2017). Relationships between gravity waves observed at Earth's surface and in the stratosphere over the central and eastern United States. *Journal of Geophysical Research: Atmospheres*, *122*(21), 11482–11498. https://doi.org/10.1002/2017JD027159

Ding, F., Wan, W., Mao, T., Wang, M., Ning, B., Zhao, B., & Xiong, B. (2014). Ionospheric response to the shock and acoustic waves excited by the launch of the Shenzhou 10 spacecraft. *Geophysical Research Letters*, *41*, 3351–3358. https://doi.org/10.1002/2014GL060107

Ding, F., Wan, W., Ning, B., & Wang, M. (2007). Larger-scale traveling ionospheric disturbances observed by GPS total electron content during the magnetic storm of 29–30 October 2003. *Journal of Geophysical Research*, *112*(A6), A06309. https://doi.org/10.1029/2006JA012013

Evans, M. (2010). An examination of low CAPE/high shear severe convective events in the Binghamton, New York county warning area. *National Weather Digest*, *34*, 129–144.

Frissell, N. A., Baker, J. B. H., Ruohoniemi, J. M., Gerrard, A. J., Miller, E. S., Marini, J. P., & Bristow, W. A. (2014). Climatology of medium-scale traveling ionospheric disturbances observed by the midlatitude blackstone superDARN radar. *Journal of Geophysical Research: Space Physics*, *119*(9), 7679–7697. https://doi.org/10.1002/2014JA019870

Fritts, D. C., & Alexander, M. J. (2003). Gravity wave dynamics and effects in the middle atmosphere. *Reviews of Geophysics*, *41*, 1003. https://doi.org/10.1029/2001RG000106

Fritts, D. C., & Vadas, S. L. (2008). Gravity wave penetration into the thermosphere: Sensitivity to solar cycle variations and mean winds. *Annals of Geophysics*, *26*(12), 3841–3861. https://doi.org/10.5194/angeo-26-3841-2008

Galvan, D. A., Komjathy, A., Hickey, M. P., Stephens, P., Snively, J., Tony Song, Y., et al. (2012). Ionospheric signatures of Tohoku-Oki tsunami of March 11, 2011: Model comparisons near the epicenter. *Radio Science*, *47*(4), RS4003. https://doi.org/10.1029/2012RS005023

Gelaro, R., McCarty, W., Suárez, J. M., Todling, R., Molod, A., Takacs, L., et al. (2017). The Modern-Era Retrospective Analysis for Research and Applications, Version 2 (MERRA-2). *Journal of Climate*, *30*(14), 5419–5454. https://doi.org/10.1175/JCLI-D-16-0758.1

Heale, C. J., Bossert, K., & Vadas, S. L. (2022). 3D numerical simulation of secondary wave generation from mountain wave breaking over Europe. *Journal of Geophysical Research: Atmospheres*, *127*(5), e2021JD035413. https://doi.org/10.1029/2021JD035413

Heale, C. J., Inchin, P. A., & Snively, J. B. (2022). Primary versus secondary gravity wave responses at F-region heights generated by a convective source. *Journal of Geophysical Research: Space Physics*, *127*(1), e2021JA029947. https://doi.org/10.1029/2021JA029947

Heale, C. J., Snively, J. B., Hickey, M. P., & Ali, C. J. (2014). Thermospheric dissipation of upward propagating gravity wave packets. *Journal of Geophysical Research*, *119*(5), 3857–3872. https://doi.org/10.1002/2013JA019387

Hernández-Pajares, M., Juan, J. M., & Sanz, J. (2006). Medium-scale traveling ionospheric disturbances affecting GPS measurements: Spatial and temporal analysis. *Journal of Geophysical Research*, *111*(A7), A07S11. https://doi.org/10.1029/2005JA011474

Hernández-Pajares, M., Juan, J. M., Sanz, J., & Orús, R. (2007). Second-order ionospheric term in GPS: Implementation and impact on geodetic estimates. *Journal of Geophysical Research*, *112*(B8), B08417. https://doi.org/10.1029/2006JB004707

Hickey, M. P., & Cole, K. D. (1981). A numerical model for gravity wave dissipation in the thermosphere. *Journal of Atmospheric and Terrestrial Physics*, *50*(8), 689–697. https://doi.org/10.1016/0021-9169(88)90032-3

Hickey, M. P., Schubert, G., & Walterscheid, R. L. (2009). The propagation of tsunami-driven gravity waves into the thermosphere and ionosphere. *Journal of Geophysical Research*, *114*(A08), 304. https://doi.org/10.1029/2009JA014105

Hines, C. O. (1960). Internal atmospheric gravity waves at ionospheric heights. *Canadian Journal of Physics*, *38*(11), 1441–1481. https://doi.org/10.1139/p60-150

Hines, C. O. (1964). Correction to internal atmospheric gravity waves at ionospheric heights. *Canadian Journal of Physics*, *42*(7), 1424–1427. https://doi.org/10.1139/p64-129

Hocke, K., & Schlegel, K. (1996). A review of atmospheric gravity waves and traveling ionospheric disturbances: 1982–1995. *Annals of Geophysics*, *14*(9), 917–940. https://doi.org/10.1007/s005850050357

Hoffmann, L. (2021). AIRS/Aqua observations of gravity waves [Dataset]. *AIRS/Aqua Observations of Gravity Waves*. https://doi.org/10.26165/JUELICH-DATA/LQAAJA

Hoffmann, L., & Alexander, M. J. (2010). Occurrence frequency of convective gravity waves during the North American thunderstorm season. *Journal of Geophysical Research*, *115*(D20), D20111. https://doi.org/10.1029/2010JD014401

Hoffmann, L., Alexander, M. J., Clerbaux, C., Grimsdell, A. W., Meyer, C. I., Rößler, T., & Tournier, B. (2014). Intercomparison of stratospheric gravity wave observations with AIRS and IASI. *Atmospheric Measurement Techniques*, *7*(12), 4517–4537. https://doi.org/10.5194/amt-7-4517-2014

Hoffmann, L., Spang, R., Orr, A., Alexander, M. J., Holt, L. A., & Stein, O. (2017). A decadal satellite record of gravity wave activity in the lower stratosphere to study polar stratospheric cloud formation. *Atmospheric Chemistry and Physics*, *17*(4), 2901–2920. https://doi.org/10.5194/acp-17-2901-2017

Hoffmann, L., Xue, X., & Alexander, M. J. (2013). A global view of stratospheric gravity wave hotspots located with Atmospheric Infrared Sounder observations. *Journal of Geophysical Research: Atmospheres*, *118*(2), 416–434. https://doi.org/10.1029/2012JD018658

Holton, J. R., & Hakim, G. J. (2013). *An introduction to dynamic meteorology*. Academic Press.

Hooke, W. H. (1968). Ionospheric irregularities produced by internal atmospheric gravity waves. *Journal of Atmospheric and Terrestrial Physics*, *30*(5), 795–823. https://doi.org/10.1016/s0021-9169(68)80033-9

Hoskins, B. J., & Hodges, K. I. (2002). New perspectives on the northern hemisphere winter storm tracks. *Journal of the Atmospheric Sciences*, *59*(6), 1041–1061. https://doi.org/10.1175/1520-0469(2002)059<1041:NPOTNH>2.0.CO;2

Hung, R. J., & Kuo, J. P. (1978). Ionospheric observation of gravity-waves associated with Hurricane Eloise. *Journal of Geophysics*, *45*, 67–80. Retrieved from https://n2t.net/ark:/88439/y031553

Hunsucker, R. D. (1982). Atmospheric gravity waves generated in the high-latitude ionosphere: A review. *Reviews of Geophysics*, *20*(2), 293–315. https://doi.org/10.1029/RG020i002p00293

Kakinami, Y., Yamamoto, M., Chen, C.-H., Watanabe, S., Lin, C., Liu, J.-Y., & Habu, H. (2013). Ionospheric disturbances induced by a missile launched from North Korea on 12 December 2012. *Journal of Geophysical Research: Space Physics*, *118*(8), 5184–5189. https://doi.org/10.1002/jgra.50508

Kelley, M. C., & Miller, C. A. (1997). Electrodynamics of midlatitude spread F, 3. Electrohydrodynamic waves? A new look at the role of electric fields in thermospheric wave dynamics. *Journal of Geophysical Research*, *102*(A6), 11539–11547. https://doi.org/10.1029/96ja03841

Kim, S.-Y., Chun, H.-Y., & Wu, D. (2009). A study on stratospheric gravity waves generated by Typhoon Ewiniar: Numerical simulations and satellite observations. *Journal of Geophysical Research*, *114*(D22), D22104. https://doi.org/10.1029/2009JD011971

Kogure, M., Chou, M. Y., Yue, J., Otsuka, Y., Liu, H., Sassi, F., et al. (2024). Medium-scale traveling ionospheric disturbances created by primary gravity waves generated by a winter storm. *Journal of Space Weather and Space Climate*, *14*, 38. https://doi.org/10.1051/swsc/2024036

Kogure, M., & Liu, H. (2021). DW1 tidal enhancements in the equatorial MLT during 2015 El Niño: The relative role of tidal heating and propagation. *Journal of Geophysical Research: Space Physics*, *126*(7), e2021JA029342. https://doi.org/10.1029/2021JA029342

Kogure, M., Liu, H., & Jin, H. (2023). Impact of tropospheric ozone modulation due to El Niño on tides in the MLT. *Geophysical Research Letters*, *50*(6), e2023GL102790. https://doi.org/10.1029/2023GL102790

Kogure, M., Nakamura, T., Murphy, D. J., Taylor, M. J., Zhao, Y., Pautet, P.-D., et al. (2023). Characteristics of gravity wave horizontal phase velocity spectra in the mesosphere over the Antarctic stations, Syowa and Davis. *Journal of Geophysical Research: Atmospheres*, *128*(6), e2022JD037751. https://doi.org/10.1029/2022JD037751

Kogure, M., & Otsuka, Y. (2025a). Detrended TEC data in 2022 (January to February) [Dataset]. *Detrended TEC data in 2022 (January to February)*. Retrieved from https://zenodo.org/records/14625201,zenodo,V2

Kogure, M., & Otsuka, Y. (2025b). Detrended TEC data in 2022 (March and April) [Dataset]. *Detrended TEC data in 2022 (March and April)*. Retrieved from https://zenodo.org/records/14625725,Zenodo,V1

Kogure, M., & Otsuka, Y. (2025c). Detrended TEC data in 2022 (may and June) [Dataset]. *Detrended TEC data in 2022 (May and June)*. Retrieved from https://zenodo.org/records/14625733,Zenodo,V1

Kogure, M., & Otsuka, Y. (2025d). Detrended TEC data in 2022 (July and August) [Dataset]. *Detrended TEC data in 2022 (July and August)*. Retrieved from https://zenodo.org/records/14625750,Zenodo,V1

Kogure, M., & Otsuka, Y. (2025e). Detrended TEC data in 2022 (September and October) [Dataset]. *Detrended TEC data in 2022 (September and October)*. Retrieved from https://zenodo.org/records/14625756,Zenodo,V1

Kogure, M., & Otsuka, Y. (2025f). Detrended TEC data in 2022 (November and December) [Dataset]. *Detrended TEC data in 2022 (November and December)*. Retrieved from https://zenodo.org/records/14625777,Zenodo,V1

Kogure, M., Yue, J., Nakamura, T., Hoffmann, L., Vadas, S. L., Tomikawa, Y., et al. (2020). First direct observational evidence for secondary gravity waves generated by mountain waves over the Andes. *Geophysical Research Letters*, *47*(17), e2020GL088845. https://doi.org/10.1029/2020GL088845

Kotake, N., Otsuka, Y., Ogawa, T., Tsugawa, T., & Saito, A. (2007). Statistical study of medium-scale traveling ionospheric disturbances observed with the GPS networks in Southern California. *Earth Planets and Space*, *59*(2), 95–102. https://doi.org/10.1186/BF03352681

Landsea, C. W. (1993). A climatology of intense (or major) Atlantic hurricanes. *Monthly Weather Review*, *121*(6), 1703–1713. https://doi.org/10.1175/1520-0493(1993)121<1703:ACOIMA>2.0.CO;2

Li, Y. Q., Jacobson, A. R., Carlos, R. C., Massey, R. S., Taranenko, Y. N., & Wu, G. (1994). The blast wave of the shuttle plume at ionospheric heights. *Geophysical Research Letters*, *21*(24), 2723–2740. https://doi.org/10.1029/94GL02548

Lin, C. H., Lin, J. T., Chen, C. H., Liu, J. Y., Sun, Y. Y., Kakinami, Y., et al. (2014). Ionospheric shock waves triggered by rockets. *Annales de Geophysique*, *32*(9), 1145–1152. https://doi.org/10.5194/angeo-32-1145-2014

Lin, C. H., Shen, M.-H., Chou, M.-Y., Chen, C.-H., Yue, J., Chen, P.-C., & Matsumura, M. (2017). Concentric traveling ionospheric disturbances triggered by the launch of a SpaceX Falcon 9 rocket. *Geophysical Research Letters*, *44*(15), 7578–7586. https://doi.org/10.1002/2017GL074192

Liu, H., Sun, Y.-Y., Miyoshi, Y., & Jin, H. (2017). ENSO effects on MLT diurnal tides: A 21 year reanalysis data-driven GAIA model simulation. *Journal of Geophysical Research: Space Physics*, *122*(5), 5539–5549. https://doi.org/10.1002/2017JA024011

Liu, H.-L., Bardeen, C. G., Foster, B. T., Lauritzen, P., Liu, J., Lu, G., et al. (2018). Development and validation of the Whole atmosphere community climate model with thermosphere and ionosphere extension (WACCM-X 2.0). *Journal of Advances in Modeling Earth Systems*, *10*(2), 381–402. https://doi.org/10.1002/2017MS001232

Liu, H.-L., McInerney, J. M., Santos, S., Lauritzen, P. H., Taylor, M. A., & Pedatella, N. M. (2014). Gravity waves simulated by high-resolution Whole atmosphere community climate model. *Geophysical Research Letters*, *41*(24), 9106–9112. https://doi.org/10.1002/2014GL062468

Liu, J.-Y., Chen, C.-H., Lin, C.-H., Tsai, H.-F., Chen, C.-H., & Kamogawa, M. (2011). Ionospheric disturbances triggered by the 11 March 2011 M9.0 Tohoku earthquake. *Journal of Geophysical Research*, *116*(A6), A06319. https://doi.org/10.1029/2011JA016761

Ma, C., & Chang, E. K. M. (2017). Impacts of storm-track variations on wintertime extreme weather events over the continental United States. *Journal of Climate*, *30*(12), 4601–4624. https://doi.org/10.1175/JCLI-D-16-0560.1

Matzka, J., Bronkalla, O., Tornow, K., Elger, K., & Stolle, C. (2021). Geomagnetic Kp index. V. 1.0. [Dataset]. *GFZ Data Services*. https://doi.org/10.5880/Kp.0001

McClintock, W. E., Rusch, D. W., Thomas, G. E., Merkel, A. W., Lankton, M. R., Drake, V. A., et al. (2009). The cloud imaging and particle size experiment on the Aeronomy of Ice in the mesosphere mission: Instrument concept, design, calibration, and on-orbit performance. *Journal of Atmospheric and Solar-Terrestrial Physics*, *71*(3–4), 340–355. https://doi.org/10.1016/j.jastp.2008.10.011

Miller, C., Swartz, W., Kelley, M., Mendillo, M., Nottingham, D., Scali, J., & Reinisch, B. (1997). Electrodynamics of midlatitude spread F: 1. Observations of unstable, gravity wave-induced ionospheric electric fields at tropical latitudes. *Journal of Geophysical Research*, *102*(A6), 11521–11532. https://doi.org/10.1029/96JA03839

Miyoshi, Y., Jin, H., Fujiwara, H., & Shinagawa, H. (2018). Numerical study of traveling ionospheric disturbances generated by an upward propagating gravity wave. *Journal of Geophysical Research: Space Physics*, *123*(3), 2141–2155. https://doi.org/10.1002/2017JA025110

Nicolls, M. J., Vadas, S. L., Aponte, N., & Sulzer, M. P. (2014). Horizontal wave parameters of daytime thermospheric gravity waves and E-region neutral winds over Puerto Rico. *Journal of Geophysical Research*, *119*, 576–600. https://doi.org/10.1002/2013JA018988

Nishioka, M., Tsugawa, T., Kubota, M., & Ishii, M. (2013). Concentric waves and short period oscillations observed in the ionosphere after the 2013 Moore EF5 tornado. *Geophysical Research Letters*, *40*(21), 5581–5586. https://doi.org/10.1002/2013GL057963

Noble, S. T. (1990). A large-amplitude traveling ionospheric disturbance excited by the Space Shuttle during launch. *Journal of Geophysical Research*, *95*(A11), 19037–19044. https://doi.org/10.1029/JA095iA11p19037

Oliver, W. L., Otsuka, Y., Sato, M., Takami, T., & Fukao, S. (1997). A climatology of F region gravity wave propagation over the middle and upper atmosphere radar. *Journal of Geophysical Research*, *102*(A7), 14499–14512. https://doi.org/10.1029/97JA00491

Otsuka, Y. (2021). Medium-scale traveling ionospheric disturbances. In C. Huang, G. Lu, Y. Zhang, & L. J. Paxton (Eds.), *Ionosphere Dynamics and Applications*. https://doi.org/10.1002/9781119815617.ch18

Otsuka, Y., Onoma, F., Shiokawa, K., Ogawa, T., Yamamoto, M., & Fukao, S. (2007). Simultaneous observations of nighttime medium-scale traveling ionospheric disturbances and E region field-aligned irregularities at midlatitude. *Journal of Geophysical Research*, *112*(A6), A06317. https://doi.org/10.1029/2005JA011548

Otsuka, Y., Shinbori, A., Tsugawa, T., & Nishioka, M. (2021). Solar activity dependence of medium-scale traveling ionospheric disturbances using GPS receivers in Japan. *Earth Planets and Space*, *73*(1), 22. https://doi.org/10.1186/s40623-020-01353-5

Perkins, F. (1973). Spread Fandionosphericcurrents. *Journal of Geophysical Research*, *78*(1), 218–226. https://doi.org/10.1029/ja078i001p00218

Pfister, L., Chan, K. R., Bui, T. P., Bowen, S., Legg, M., Gary, B., et al. (1993). Gravity waves generated by a tropical cyclone during the step tropical field program: A case study. *Journal of Geophysical Research*, *98*(D5), 8611–8638. https://doi.org/10.1029/92JD01679

Pfister, L., & Russell, P. B. (1993). Preface [to special section on 'the tropical experiment of the stratosphere-troposphere Exchange project (STEP tropical)]. *Journal of Geophysical Research*, *98*(D5), 8561–8562. https://doi.org/10.1029/93JD00860

Piani, C., Durran, D., Alexander, M. J., & Holton, J. R. (2000). A numerical study of three-dimensional gravity waves triggered by deep tropical convection and their role in the dynamics of the QBO. *Journal of the Atmospheric Sciences*, *57*(22), 3689–3702. https://doi.org/10.1175/1520-0469(2000)057<3689:ANSOTD>2.0.CO;2

Randall, C. E., Carstens, J., France, J. A. J., Harvey, V. L., Hoffmann, L., Bailey, S. M., et al. (2017). New AIM/CIPS global observations of gravity waves near 50–55 km [Dataset]. *Geophysical Research Letters*, *44*(13), 7044–7052. https://doi.org/10.1002/2017GL073943

Richmond, A. D. (1978). Gravity wave generation, propagation, and dissipation in the thermosphere. *Journal of Geophysical Research*, *83*(A9), 4131–4145. https://doi.org/10.1029/JA083iA09p04131

Rusch, D., Thomas, G., Merkel, A., Olivero, J., Chandran, A., Lumpe, J., et al. (2017). Large ice particles associated with small ice water content observed by AIM CIPS imagery of polar mesospheric clouds: Evidence for microphysical coupling with small-scale dynamics. *Journal of Atmospheric and Solar-Terrestrial Physics*, *162*, 97–105. https://doi.org/10.1016/j.jastp.2016.04.018

Russell, J. M., III., Bailey, S. M., Gordley, L. L., Rusch, D. W., Horanyi, M., Herving, M. E., et al. (2009). Aeronomy of ice in the mesosphere (AIM): Overview and early science results. *Journal of Atmospheric and Solar-Terrestrial Physics*, *71*(3–4), 289–299. https://doi.org/10.1016/j.jastp.2008.08.011

Saito, A., Iyemori, T., Blomberg, L. G., Yamamoto, M., & Takeda, M. (1998). Conjugate observations of the mid-latitude electric field fluctuations with the MU radar and the Freja satellite. *Journal of Atmospheric and Solar-Terrestrial Physics*, *60*(1), 129–140. https://doi.org/10.1016/S1364-6826(97)00094-1

Samson, J. C., Greenwald, R. A., Ruohoniemi, J. M., & Baker, K. B. (1989). High-frequency radar observations of atmospheric gravity waves in the high-latitude ionosphere. *Geophysical Research Letters*, *16*(8), 875–878. https://doi.org/10.1029/GL016i008p00875

Sassi, F., Liu, H.-L., Ma, J., & Garcia, R. R. (2013). The lower thermosphere during the northern hemisphere winter of 2009: A modeling study using high-altitude data assimilation products in WACCM-X. *Journal of Geophysical Research: Atmospheres*, *118*(16), 8954–8968. https://doi.org/10.1002/jgrd.50632

Sherburn, K. D., & Parker, M. D. (2014). Climatology and ingredients of significant severe convection in high-shear, low-CAPE environments. *Weather and Forecasting*, *29*(4), 854–877. https://doi.org/10.1175/WAF-D-13-00041.1

Shiokawa, K., Otsuka, Y., Ihara, C., Ogawa, T., & Rich, F. J. (2003). Ground and satellite observations of nighttime medium-scale traveling ionospheric disturbance at midlatitude. *Journal of Geophysical Research*, *108*(A4), 1145. https://doi.org/10.1029/2002JA009639

Srinivasu, V. K. D., & Dashora, N. (2024). Multi-altitude observations of the lower atmospheric disturbances and its ionospheric signatures over the Indian region. *Advances in Space Research*, *73*(7), 3435–3451. https://doi.org/10.1016/j.asr.2023.06.001

Takahashi, H., Figueiredo, C. A. O. B., Essien, P., Wrasse, C. M., Barros, D., Nyassor, P. K., et al. (2022). Signature of gravity wave propagations from the troposphere to ionosphere. *Annales Geophysicae*, *40*(6), 665–672. https://doi.org/10.5194/angeo-40-665-2022

Taylor, M. J., & Hapgood, M. A. (1988). Identification of a thunderstorm as a source of short period gravity waves in the upper atmospheric nightglow emissions. *Planetary and Space Science*, *36*(10), 975–985. https://doi.org/10.1016/0032-0633(88)90035-9

Tsugawa, T., Saito, A., & Otsuka, Y. (2004). A statistical study of large-scale traveling ionospheric disturbances using the GPS network in Japan. *Journal of Geophysical Research*, *109*(A6), A06302. https://doi.org/10.1029/2003JA010302

Uccelini, L. W. (1990). Processes contributing to the rapid development of extratropical cyclones. In C. W. Newton & E. O. Holopainen (Eds.), *Extratropical cyclones*. American Meteorological Society. https://doi.org/10.1007/978-1-944970-33-8_6

Vadas, S. L. (2007). Horizontal and vertical propagation and dissipation of gravity waves in the thermosphere from lower atmospheric and thermospheric sources. *Journal of Geophysical Research*, *112*(A6), A06305. https://doi.org/10.1029/2006JA011845

Vadas, S. L. (2013). Compressible f-plane solutions to body forces, heatings, and coolings, and application to the primary and secondary gravity waves generated by a deep convective plume. *Journal of Geophysical Research: Space Physics*, *118*(5), 2377–2397. https://doi.org/10.1002/jgra.50163

Vadas, S. L., & Azeem, I. (2021). Concentric secondary gravity waves in the thermosphere and ionosphere over the continental United States on March 25–26, 2015 from deep Convection. *Journal of Geophysical Research: Space Physics*, *126*(2), e2020JA028275. https://doi.org/10.1029/2020JA028275

Vadas, S. L., & Becker, E. (2019). Numerical modeling of the generation of tertiary gravity waves in the mesosphere and thermosphere during strong mountain wave events over the southern Andes. *Journal of Geophysical Research: Space Physics*, *124*(9), 7687–7718. https://doi.org/10.1029/2019JA026694

Vadas, S. L., & Crowley, G. (2010). Sources of the traveling ionospheric disturbances observed by the ionospheric TIDDBIT sounder near wallops island on 30 October 2007. *Journal of Geophysical Research*, *115*(A7), A07324. https://doi.org/10.1029/2009JA015053

Vadas, S. L., Figueiredo, C., Becker, E., Huba, J. D., Themens, D. R., Hindley, N., et al. (2023). Traveling ionospheric disturbances induced by the secondary gravity waves from the Tonga eruption on 15 January 2022: Modeling with MESORAC-HIAMCM-SAMI3 and comparison with GPS/TEC and ionosonde data. *Journal of Geophysical Research: Space Physics*, *128*(6), e2023JA031408. https://doi.org/10.1029/2023JA031408

Vadas, S. L., & Fritts, D. C. (2004). Thermospheric responses to gravity waves arising from mesoscale convective complexes. *Journal of Atmospheric and Solar-Terrestrial Physics*, *66*(6–9), 781–804. https://doi.org/10.1016/j.jastp.2004.01.025

Vadas, S. L., & Fritts, D. C. (2005). Thermospheric responses to gravity waves: Influences of increasing viscosity and thermal diffusivity. *Journal of Geophysical Research*, *110*(D15), D15103. https://doi.org/10.1029/2004JD005574

Vadas, S. L., & Fritts, D. C. (2006). Influence of solar variability on gravity wave structure and dissipation in the thermosphere from tropospheric convection. *Journal of Geophysical Research*, *111*(A10), A10S12. https://doi.org/10.1029/2005JA011510

Vadas, S. L., & Liu, H. (2009). Generation of large-scale gravity waves and neutral winds in the thermosphere from the dissipation of convectively generated gravity waves. *Journal of Geophysical Research*, *114*(A10), A10310. https://doi.org/10.1029/2009JA014108

Vadas, S. L., & Liu, H.-L. (2013). Numerical modeling of the large-scale neutral and plasma responses to the body forces created by the dissipation of gravity waves from 6 h of deep convection in Brazil. *Journal of Geophysical Research: Space Physics*, *118*(5), 2593–2617. https://doi.org/10.1002/jgra.50249

Vadas, S. L., Yue, J., She, C.-Y., Stamus, P. A., & Liu, A. Z. (2009). A model study of the effects of winds on concentric rings of gravity waves from a convective plume near Fort Collins on 11 May 2004. *Journal of Geophysical Research*, *114*(D6), D06103. https://doi.org/10.1029/2008JD010753

Wernli, H., Dirren, S., Liniger, M. A., & Zillig, M. (2002). Dynamical aspects of the life cycle of the winter storm “Lothar” (24–26 December 1999). *The Quarterly Journal of the Royal Meteorological Society*, *128*(580), 405–429. https://doi.org/10.1256/003590002321042036

Wright, C. J., Hindley, N. P., Alexander, M. J., Barlow, M., Hoffmann, L., Mitchell, C. N., et al. (2022). Surface-to-space atmospheric waves from Hunga Tonga–Hunga Ha’apai eruption. *Nature*, *609*(7928), 741–746. https://doi.org/10.1038/s41586-022-05012-5

Xu, S., Carstens, J. N., France, J. A., Randall, C. E., Yue, J., Harvey, V. L., et al. (2024). Seasonal distribution of gravity waves near the stratopause in 2019–2022. *Earth and Space Science*, *11*(1), e2023EA003076. https://doi.org/10.1029/2023EA003076

Yang, Z., Gu, S.-Y., Qin, Y., Teng, C.-K., Huang, F., Sun, W., & Dou, X. (2022). Statistical study of F-region short period ionospheric disturbances related to convection in the lower atmosphere over Wuhan, China. *Space Weather*, *20*(10), e2022SW003140. https://doi.org/10.1029/2022SW003140

Yue, J., Hoffmann, L., & Joan Alexander, M. (2013). Simultaneous observations of convective gravity waves from a ground-based airglow imager and the AIRS satellite experiment. *Journal of Geophysical Research: Atmospheres*, *118*(8), 3178–3191. https://doi.org/10.1002/jgrd.50341

Yue, J., Miller, D. S., Hoffmann, L., & Straka, C. W. (2014). Stratospheric and mesospheric concentric gravity waves over tropical cyclone Mahasen: Joint AIRS and VIIRS satellite observations. *Journal of Atmospheric and Solar-Terrestrial Physics*, *119*, 83–90. https://doi.org/10.1016/j.jastp.2014.07.003